



---

## Process-based Modelling of a Crevasse Splay

---

by  
**Axel B. Sandén**

TO OBTAIN THE DEGREE OF MASTER OF SCIENCE

DELFT UNIVERSITY OF TECHNOLOGY  
FACULTY OF CIVIL ENGINEERING AND GEOSCIENCES  
DEPARTMENT OF GEOSCIENCE & ENGINEERING  
SECTION OF APPLIED GEOLOGY

TO BE DEFENDED PUBLICLY ON MONDAY OCTOBER 24, 2016 AT 14:00

|                    |                                      |                         |
|--------------------|--------------------------------------|-------------------------|
| Student number:    | 4009142                              |                         |
| Project duration:  | November 16, 2015 - October 24, 2016 |                         |
| Thesis Committee:  | Dr. M.E. Donselaar (Chair)           | TU Delft, supervisor    |
|                    | Dr. J.E.A. Storms                    | TU Delft, co-supervisor |
|                    | Dr. K.H.A.A. Wolf                    | TU Delft                |
|                    | Drs. J.E. Lutgert                    | EBN B.V.                |
| Daily Supervisors: | K.A. van Tooreenburg, MSc.           | TU Delft                |
|                    | H. van der Vegt, MSc.                | TU Delft                |

An electronic version of this thesis is available at <http://repository.tudelft.nl>

### Abstract

Exploitation of unconventional resources could prolong the gas production in the North Sea. Low-net-to-gross fluvial intervals have tough-gas reservoir potential in thin-bedded crevasse splays. To assess economic risks associated to the development of these reservoirs, a reliable depositional model is required. Sparse areal data availability for reservoir models commonly results in the use of stochastic interpolation. Numerical models offer the possibility to support these methods with proven physical concepts. To this end, simulations were conducted with Delft3D process-based modelling software. Input parameters and the validation data sets for these models are derived from outcrop studies in the present-day Río Colorado fluvial system in the Altiplano Basin, Bolivia. In total 174 simulations were run, of which five models were analysed in detail. The model output consists of discrete morphological, hydrodynamical, and grain-size data. Petrophysical parameters were derived from continuous grain size distributions parameters. This study demonstrates a statistical approach to extract these from discrete grain-size data. A sensitivity study shows that using the right size and amount of grain-size classes is crucial to minimize errors.

Simulations demonstrate the effect of different conditions through their direct influence on physical processes. Crevasse-splay formation only occurs for water levels that are higher than the base of the levee breach and lower than the top of the levee. The resulting morphology is dependent on the relation between the driving hydrodynamic gradient and the counteracting frictional forces. Both outflow from the river onto the floodplain and reflux of water back into the river leads to an erosional channel network. Crevasse channels, together with their related overbank and mouth-bar deposits, form the architectural elements that make up crevasse splays. A quantitative comparison was made between field and simulated data. It shows that the model overestimates the grain size as sediment is transported away from a channel. The conclusion is that this model is not valid for quantitative purposes. The process-based model with its current abilities and limitations can be used as a tool for heuristic research. It allows the study of the different governing processes. These ideas should be taken back into the field to test, validate, and further study the exact morphodynamics of the system. Resulting concepts can be used to accurately predict the crevasse-splay architecture and corresponding sedimentary trends. Subsequently these can be used as an input in reservoir models to improve their reliability.

## Contents

|          |  |           |
|----------|--|-----------|
| <b>1</b> | <b>Introduction</b>  | <b>5</b>  |
| <b>2</b> | <b>Model description, setup, calibration and output processing</b> | <b>7</b>  |
| 2.1      | Model description . . . . .  | 7         |
| 2.2      | Setup . . . . .  | 8         |
| 2.2.1    | Forcing: Flooding cycles . . . . .                                 | 8         |
| 2.2.2    | Initial bathymetry . . . . .                                       | 9         |
| 2.2.3    | Sediment Input . . . . .   | 10        |
| 2.2.4    | Sediment properties . . . . .                                      | 11        |
| 2.3      | Calibration . . . . .  | 12        |
| 2.3.1    | Splay Fine (SF) models . . . . .                                   | 12        |
| 2.3.2    | Multi Run (MR) models . . . . .                                    | 13        |
| 2.3.3    | Splay Big (SB) models . . . . .                                    | 13        |
| 2.4      | Data Processing . . . . .  | 13        |
| 2.4.1    | Field data analysis . . . . .                                      | 14        |
| 2.4.2    | Model data analysis . . . . .                                      | 16        |
| 2.4.3    | Statistical error . . . . .  | 17        |
| 2.4.4    | Derivation of Porosity and Permeability . . . . .                  | 17        |
| <b>3</b> | <b>Results</b>   | <b>19</b> |
| 3.1      | Bathymetry 1 . . . . .   | 19        |
| 3.2      | Bathymetry 3 . . . . .   | 24        |
| 3.3      | Statistical Error & Sensitivity . . . . .                          | 26        |
| 3.4      | Field-data analysis . . . . .                                      | 27        |
| <b>4</b> | <b>Discussion</b>  | <b>30</b> |
| 4.1      | Crevasse splay dynamics . . . . .                                  | 30        |
| 4.1.1    | Boundary conditions . . . . .                                      | 30        |
| 4.1.2    | Crevasse-splay evolution . . . . .                                 | 30        |
| 4.2      | Crevasse-splay morphology . . . . .                                | 32        |
| 4.2.1    | Crevasse channel . . . . .   | 33        |
| 4.2.2    | Crevasse-channel-overbank deposits . . . . .                       | 35        |
| 4.2.3    | Mouth bar . . . . .  | 35        |
| 4.2.4    | Crevasse splay architecture . . . . .                              | 36        |
| 4.3      | Sedimentary trends & their relation to crevasse channels . . . . . | 37        |
| 4.4      | Compensational stacking . . . . .                                  | 39        |
| 4.5      | Petrophysical properties & Statistical error . . . . .             | 39        |
| <b>5</b> | <b>Conclusions</b>   | <b>41</b> |
| <b>6</b> | <b>Acknowledgements</b>  | <b>42</b> |
| <b>A</b> | <b>The Río Colorado fluvial fan</b>                                | <b>46</b> |
| <b>B</b> | <b>SF models</b>   | <b>47</b> |
| <b>C</b> | <b>MR models</b>   | <b>49</b> |
| <b>D</b> | <b>SB models</b>   | <b>51</b> |

|          |  |           |
|----------|--|-----------|
| <b>E</b> | <b>Cross sections MR-3 with sediment fractions</b> | <b>52</b> |
| <b>F</b> | <b>Bathymetry 2</b>                                | <b>52</b> |
| <b>G</b> | <b>Field Data analysis CS2 &amp; CS24</b>          | <b>54</b> |
| G.1      | Splay CS2 . . . . .                                | 54        |
| G.2      | CS24 . . . . .                                     | 55        |

## List of Symbols

|                           |  |
|---------------------------|--|
| $\alpha$                  | Calibration coefficient (O(1)) [-]                           |
| $\delta$                  | Relative density [-]   |
| $\Delta t$                | Time step [s]  |
| $\Delta x$                | Grid size in x direction [m]                                 |
| $\Delta y$                | Grid size in y direction [m]                                 |
| $\kappa$                  | First Weibull distribution coefficient [-]                   |
| $\lambda$                 | Second Weibull distribution coefficient[-]                   |
| $\rho_{\text{bed}}$       | Dry bed density [kg/m <sup>3</sup> ]                         |
| $\rho_{\text{spec}}$      | Specific density [kg/m <sup>3</sup> ]                        |
| $\rho_{\text{set}}$       | Reference density for hindered settling [kg/m <sup>3</sup> ] |
| $\tau_{\text{b}}$         | Bed shear stress [Pa]  |
| $\tau_{\text{cr,b}}$      | Critical bed shear stress [Pa]                               |
| $\mu$                     | Viscosity [Pa · s]   |
| $\rho_{\text{p}}$         | Particle density[kg/m <sup>3</sup> ]                         |
| $\rho_{\text{f}}$         | Fluid density [kg/m <sup>3</sup> ]                           |
| $\sigma$                  | Standard deviation [-]                                       |
| $C$                       | Chézy friction Coefficient [m <sup>0.5</sup> /s]             |
| $C_{\text{ero}}$          | Erosion parameter [kg/m <sup>2</sup> /s]                     |
| $D_{50}$                  | Median grain diameter [m]                                    |
| $D_{\text{H}}$            | Horizontal eddy diffusivity [m <sup>2</sup> /s]              |
| $D_{\text{p}}$            | Particle diameter [m]  |
| $\overline{D}_{\text{p}}$ | Mean Particle diameter [m]                                   |
| $g$                       | Gravity constant [m/s <sup>2</sup> ]                         |
| $k$                       | Permeability [m <sup>2</sup> ]                               |
| $p_{n,\text{sampled}}$    | Probability of sampled grain-size class                      |
| $S$                       | Sediment volume [m <sup>3</sup> ]                            |
| $S_{\text{b}}$            | Sediment volume, bedload [m <sup>3</sup> ]                   |
| $S_{\text{s}}$            | Sediment volume, suspended [m <sup>3</sup> ]                 |
| $U$                       | Water velocity [m/s]   |
| $V_{\text{set}}$          | Unhindered settling velocity [m/s]                           |

## 1 Introduction

The North Sea and other major mature gas provinces suffer from a decline in the production of gas from conventional reservoirs. This causes a reduction in state income and above all a dependency on other gas-producing countries. In order to secure the energy supply for the future, gas from unconventional sources such as tough reservoirs in low net-to-gross intervals will play an increasingly important role.

Tough reservoirs commonly proved to be marginally profitable. Therefore, low-cost production strategies like producing from existing infrastructure is essential. Re-perforation tests of bypassed low net-to-gross fluvial intervals indicate that they may contain significant amounts of producible gas. This marks the previously-ignored floodplain deposits as a potential future target (Donselaar et al., 2011).

Low net-to-gross fluvial reservoirs are commonly described as a labyrinth-type of reservoir (Weber and van Geuns, 1990). The individual river-channel sandstone bodies form a complex within a matrix of floodplain fines. The connectivity of the individual sandstone bodies is crucial for the performance of the reservoir. However, river channels are not the only sand-containing bodies present within the fluvial domain. Floodplains commonly contain thin-bedded sheets of very-fine to fine sand. These so-called crevasse splays are the result of levee breaches during which coarse silt and fine sand is transported onto the floodplain (Mjos et al., 1993; Bristow et al., 1999; Slingerland and Smith, 2004; Bridge, 2006).

Crevasse splays are commonly associated with the distal areas of fluvial systems (Slingerland and Smith, 2004; Tooth, 2005; Nichols and Fisher, 2007). They have also been observed in fossil and present-day braided river systems (Bristow et al., 1999). Their morphology has been described in several studies (O'Brien and Wells, 1986; Mjos et al., 1993; Rhee and Chough, 1993; Bristow et al., 1999; Li and Bristow, 2015).

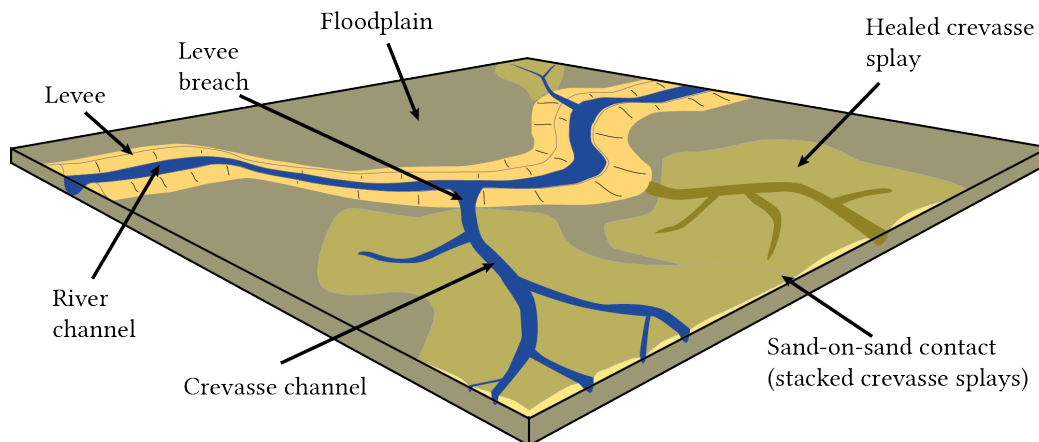


*Figure 1: Terminology concerning crevasse splays used in this report*

However, literature based its findings on field data, which fails to capture all the relevant dimensions. Outcrops and modern-day analogues miss the temporal and vertical dimension respectively. A numerical process-based model can complement these data sources by providing a 4D data set derived from physical relations. Numerical models are already used for heuristic analysis like predicting local coastal dynamics for engineering purposes (Dastgheib et al., 2008).

Currently, process-based models of floodplain deposits are embedded in architecture-scale river-channel-belt models. These models focus on river-channel deposits and tend to (over)simplify the overbank processes (Hajek and Wolinsky, 2012). Meanwhile, crevasse splays act as forerunners for avulsions in the fluvial domain (Donselaar et al., 2013; Hajek and Wolinsky, 2012; Slingerland and Smith, 1998). They are represented in more

detail in research on avulsions. Slingerland and Smith (1998) presented a one-dimensional model that predicts the stability of a crevasse splay as a function of morphology and sediment properties. Hajek and Edmonds (2014) used the Delft3D package to model the overbank behaviour of water and sediment. They proposed a correlation between sandiness of the floodplain and among others the erodibility of the substrate and sediment size. Both models proposed by Hajek and Wolinsky (2012) and Slingerland and Smith (1998) did not include the sediment distribution within a crevasse splay. For numerical fluid flow simulations, this can be valuable input as it influences petrophysical properties like porosity and permeability.

The aim of this study is to explore the possibilities of a process-based model to create an understanding of a crevasse splay governing processes and resulting sedimentary architecture. It presents the setup of a process-based model. The model was calibrated with data from the modern day Río Colorado fluvial system<sup>1</sup>, which serves as an analogue for the Permo-Triassic low net-to-gross intervals in the Dutch subsurface (Donselaar et al., 2013). Subsequently, the models output is processed and compared with the input data. Lastly, the validity of the process-based models is discussed.

---

<sup>1</sup>See appendix A

## 2 Model description, setup, calibration and output processing

A process-based model was created to study the morphodynamical processes and sedimentary trends of crevasse-splay deposition. The model was set and calibrated using data from a modern day fluvial system (fig. 2). Quantitative data sets of the channel/floodplain morphology (Donselaar et al., 2013), discharge models (Li et al., 2014), and grain-size distribution in crevasse splays were used.

The model produces discrete morphological, hydrodynamical, and grain-size data. The discrete grain-size data are transposed to continuous statistical distributions using the same statistical fitting used for the analysis of the available field data. The last step was comparison of the models output with data from natural fluvial systems. The validity of the model will be tested in the discussion.

In this chapter the different elements of the workflow are presented in the following order:

1. The setup of the model.
2. The calibration of the model, including a description of the test runs.
3. The processing of both the input as the output data.

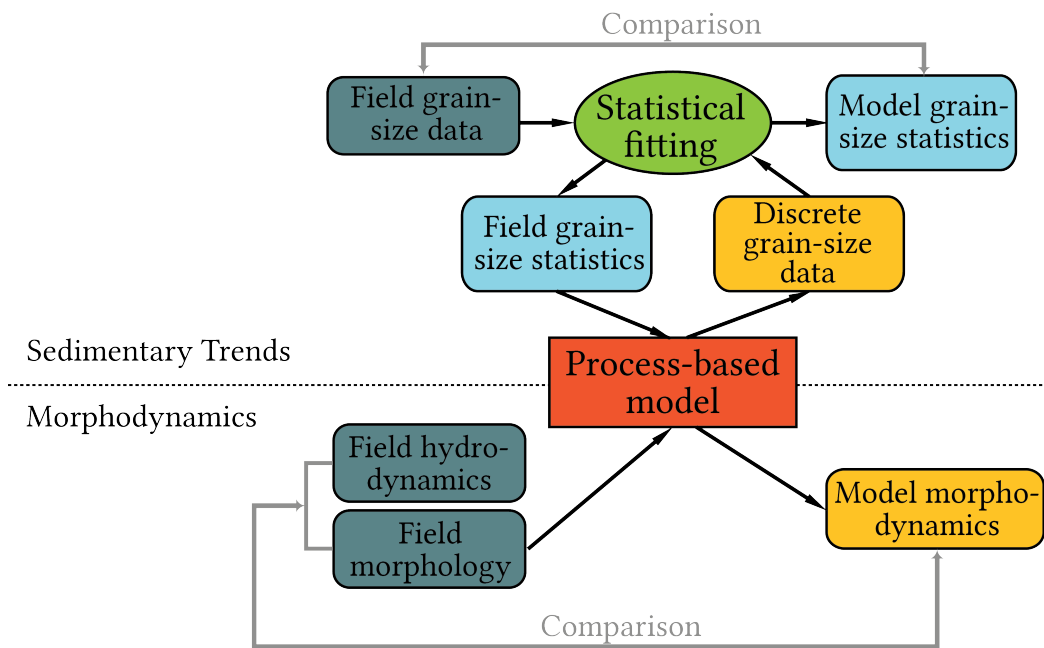


Figure 2: The workflow used in this study

### 2.1 Model description

Floodplain deposition was modelled with the 2DH version of Delft3D (Lesser et al., 2004). A 2D solution is reached by depth averaging the governing equations of the hydrodynamic 3D model. For the simulations in this thesis, a robust flooding scheme was used to solve the continuity and horizontal momentum equations (Leendertse, 1987; Lesser et al., 2004). This explicit scheme is preferred as it can handle numerical instabilities associated with the drying and flooding of individual grid cells (Stelling et al., 1986).

For sediment transport, the formulation from Engelund and Hansen (1976) was used :

$$S = S_b + S_s = \frac{0.05\alpha U^5}{\sqrt{gC^3\delta^2 D_{50}}}$$

- In which  $S$  : Total sediment transport rate [ $\text{kg} \cdot \text{m}^{-1} \cdot \text{s}^{-1}$ ],  
 $S_b$  : Bedload transport rate [ $\text{kg} \cdot \text{m}^{-1} \cdot \text{s}^{-1}$ ],  
 $S_s$  : Suspended-load transport rate [ $\text{kg} \cdot \text{m}^{-1} \cdot \text{s}^{-1}$ ],  
 $\alpha$  : Calibration coefficient [-],  
 $U$  : Magnitude of the flow velocity [ $\text{m} \cdot \text{s}^{-1}$ ],  
 $g$  : gravity constant [ $\text{m} \cdot \text{s}^{-2}$ ],  
 $C$  : Chézy friction Coefficient [ $\text{m}^{0.5} \cdot \text{s}^{-1}$ ],  
 $\delta$  : Relative density [-],  
 $D_{50}$  : Median grain size diameter [m]

This is an empirically derived correlation which has been frequently used in rivers and estuaries. The ratio between the bed- and suspended-load transport rate is a pre-set value. The formula shows that transport capacity for a given grain diameter increases with a fifth power of the water velocity.

The magnitude and direction of the bed-load and suspended-load transport rates are calculated by solving an advection-diffusion equation. Subsequently, the transport rates are corrected for the bed-slope effect (only bed load), upwind bed composition, and sediment availability. The resulting transport rates at the cell interfaces are used to redistribute four discrete sediment classes. For erosion and deposition, the sub-layer concept is used. The sediment volume fractions are stored in a 3D grid, in which sedimentation and erosion are restricted to the uppermost (transport) layer.

## 2.2 Setup

The simulation of a single crevasse splay is set in a uniform Cartesian grid with  $m \times n$  grid-cells that have an individual size of 2x2 meter (fig. 3). On the left side of the model, a river channel laterally confined by two levees. Water flows in at the bottom ( $y=0$ ) and flows out at the top ( $y = 500$ ). There is a weak spot in the middle of the right levee, which acts as a preferred breach point. On the right of the right levee an almost flat (angle  $< 0.005^\circ$ ) floodplain is situated.

### 2.2.1 Forcing: Flooding cycles

Field observations show that crevasses are formed by one or multiple flooding events (Donselaar et al., 2013). An event can be separated in five distinct stages (fig. 4):

1. **Confined flow** Flow is confined to the river channel below the base of the levee breach.
2. **Crevasse formation** The water level increases until bankfull. Locally, this results in levee breakthrough.
3. **Floodplain inundation** Water level exceeds levee height, resulting in unconfined flow on the floodplain.
4. **Reflux** Water level drops and water flows back from the floodplain back into the river channel.
5. **Evaporation & Percolation** The last water is drained from the floodplain.

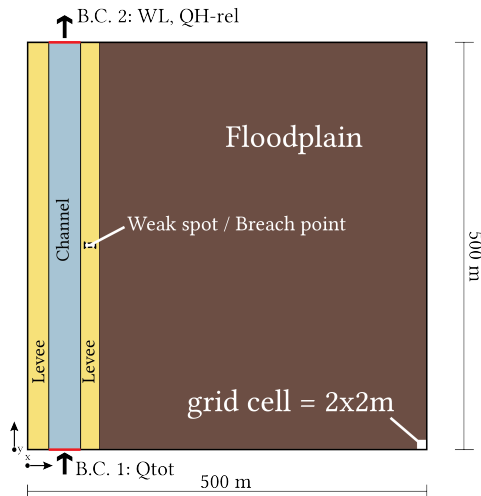


Figure 3: The model setup showing a 500x500m domain. On the right side the floodplain is situated. On the left the river channel with two adjacent levees with in middle of the right levee the weak point.

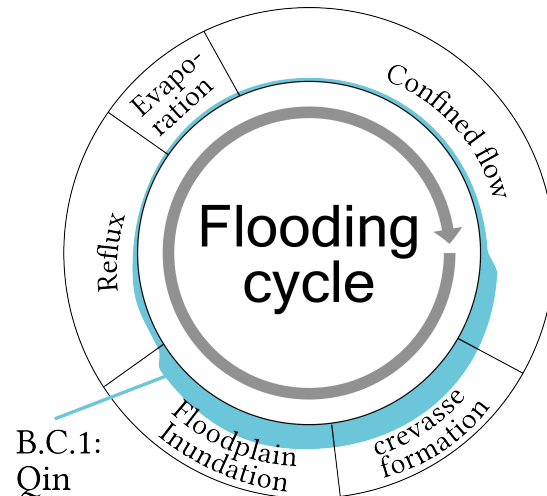


Figure 4: Concept of the flooding cycle showing the different stages and a qualitative magnitude of the first boundary condition (B.C. 1)

The main forces steering these processes is primarily the discharge, and secondarily the evaporation and percolation. An increased discharge will result in crevassing and, ultimately, inundation. When run-off decreases, part of the water flows back into the river channel, after which evaporation and percolation start to dominate (fig. 4). Crevasse splays are formed during one or more of these cycles. Hence, they serve as a guideline for setting the boundary conditions.

The model was forced by two boundary conditions controlling the inflow and outflow of water and sediment. The outflow condition is a water level/discharge relation, meaning that for a given discharge at the boundary the water-level is set to a predefined value. The inflow is steered by a discrete time series, where at each time the discharge is set. Evaporation is set as a force acting on the whole grid. It captures the effect of evaporation and percolation combined.

The values for the boundary conditions were calibrated so that the model honours the flooding cycle. If the discharge is too high, it will directly inundate the floodplain and skip the crevasse-formation step. Conversely, if the evaporation is set too low, the floodplain will still hold water when the the next flooding occurs.

### 2.2.2 Initial bathymetry

Channel geometry was set using data gathered from the Río Colorado fluvial system. Proximally to distally, the system shows a decrease in topographic height and a decreasing cross-sectional area of the river channel. The distal area of interest has a river depth and width ranging from 0.6 - 1.2 and 10 - 20 meters respectively (Donselaar et al., 2013). Levee and floodplain morphology was derived from differential GPS height measurements along different sections perpendicular to the river channel. To model natural heterogeneity of the floodplain a random value was added, which was drawn from a uniform distribution between 0 and 2 cm.

From this data two channel-levee-floodplain profiles were constructed. (fig. 5). Subsequently, using these two profiles, three different initial bathymetries were created (fig.6).

1. Bathymetry 1: a river channel cutting into a flat floodplain (fig.6 B1).
2. Bathymetry 2: A more mature version of this river channel. It has aggraded and ongoing overbank and

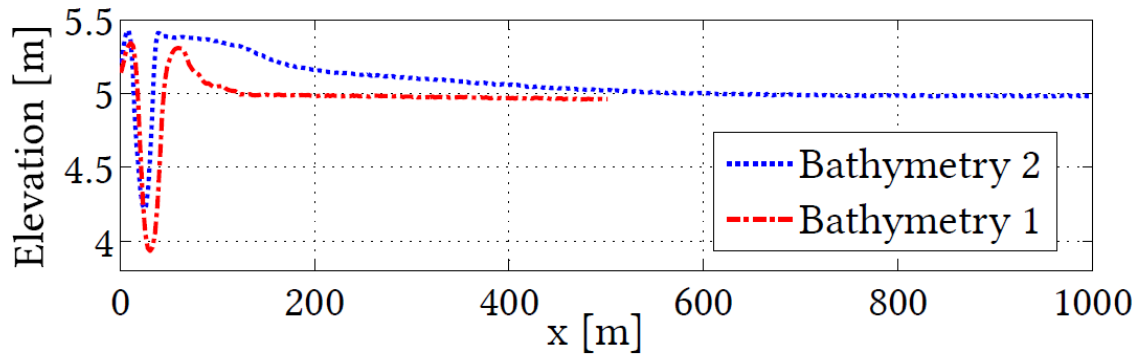


Figure 5: Cross sections perpendicular to the river channel showing the initial bathymetry

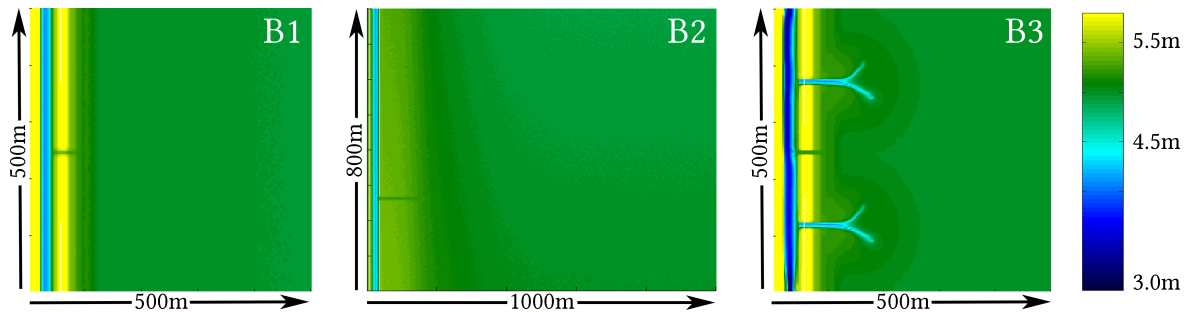


Figure 6: Surface plot of the three initial bathymetries (B1,B2,B3)

crevasse-splay deposition created a floodplain showing more relief (fig.6 B2).

3. Bathymetry 3: An evolution state between bathymetry 1 & 2. The floodplain profile is similar to bathymetry one. However, two existing crevasse splays are situated lateral to the breach point. The morphology and sediment composition of these crevasse splays are derived from model output that uses Bathymetry 1 as its original profile. The goal of this bathymetry is to study compensational stacking (Li et al., 2014) (fig.6 B3).

### 2.2.3 Sediment Input

Sediment input is chosen such that it represents the sediment distribution of available field data. The following considerations have been taken into account:

- The average grain size from a crevasse splay is smaller than the sediment present in the river channel (van Toorenburg et al., 2016). Hence, the field data are expected to be an underestimation of the original composition of the river's sediment load.
- The discrete grain-size classes should capture the two main sediment fractions observed in the field data.

Two discrete sets of sediment classes have been used. The first set is based on grain-size distributions from the Río Colorado fluvial fan (Torres Carranza, 2013). The second set is based on the Huesca fluvial fan (van Toorenburg et al., 2016), which contains comparatively coarser sediment (table 1).

|         | Sediment Classes             | Substrate Composition | Used in model                |
|---------|------------------------------|-----------------------|------------------------------|
| Set 1   | 7, 25, 64, 110 $\mu\text{m}$ | 25%,25%,25%,25%       | MR-1                         |
| Set 2.1 | 7, 25, 45, 80 $\mu\text{m}$  | 25%,25%,25%,25%       | MR-2, MR-2COMP-1, MR-2COMP-2 |
| Set 2.2 | 7, 25, 45, 80 $\mu\text{m}$  | 20%,50%,20%,10%       | MR-3                         |

Table 1: Sediment classes and substrate composition for the three analysed models. Sediment set 2.1 & sediment set 2.2 have the grain-size set based on the Río Colorado fluvial fan field data. sediment set 1 has grain-size set based on the Huesca fluvial fan field data.

## 2.2.4 Sediment properties

The model distinguishes two types of sediment (cohesive and non-cohesive), both with different required input parameters (table 2). In practice these two classes are discriminated based on their grain-size. The sediment class is categorized as cohesive for a grain diameter smaller than 64  $\mu\text{m}$  and non-cohesive when larger. The behaviour of these sediments is strongly dependent on the input parameters, which represent their physical properties. The number of parameters needed for non-cohesive sediments is lower than the amount needed for cohesive sediments (table 2), as these are derived from built-in grain-size-based correlations (van Rijn, 1993).

| Cohesive                 |   | Non-Cohesive         |                          |
|--------------------------|---|----------------------|--------------------------|
| $\rho_{\text{spec}}$     | Specific density                            | $\rho_{\text{spec}}$ | Specific density         |
| $V_{\text{set}}$         | Settling velocity fresh water               | $D_{50}$             | Median sediment diameter |
| $\tau_{\text{cr,b,sed}}$ | Critical bed shear stress for sedimentation | $\rho_{\text{bed}}$  | Dry bed density          |
| $\tau_{\text{cr,b,ero}}$ | Critical bed shear stress for erosion       |                      |                          |
| $C_{\text{ero}}$         | Erosion parameter                           |                      |                          |
| $\rho_{\text{bed}}$      | Dry bed density                             |                      |                          |

Table 2: Input parameters for (non-)cohesive sediment properties

**Critical bed shear stress** Sediment transport occurs when the fluid exerts a force that is larger than the resisting force related to the submerged particle weight and the friction coefficient (van Rijn, 2006). This resisting force is represented by a parameter called the critical bed shear stress for erosion ( $\tau_{\text{cr,b,ero}}$ ). The same principle, but reversed, is used for sedimentation where a critical bed shear stress of sedimentation is defined so that sediment occurs for  $\tau_{\text{cr,b,sed}} < \tau_{\text{b}}$ .

Lab observations of the effect on pure quartz grains show that  $\tau_{\text{cr,b,ero}}$  is a function of particle size (Zanke, 2003). As soon as other minerals are present in the sediment, inter-particle forces start to play a significant role. This results in observations that for  $D_{\text{p}} < 64\mu\text{m}$  there is often a negative correlation between  $\tau_{\text{cr,b,ero}}$  and particle size (Roberts et al., 1998; Guoren, 2000). Based on the results of Roberts et al. (1998), it can be concluded that critical shear stress for silts is affected by grain size, the packing of the bed (wet bulk density), and the presence of clay particles (van Rijn, 2006).

**Settling velocity** The settling velocity of natural particles is commonly described as a function of particle geometry, density, and fluid properties (Cheng, 1997; Jiménez and Madsen, 2003). The method of van Rijn (1993) uses the formulation of Jiménez and Madsen (2003) for a representative particle diameter ( $D_{\text{s}}$ ) between 100 and 1000  $\mu\text{m}$ . For  $64\mu\text{m} < D_{\text{s}} < 100\mu\text{m}$  this formulation is in agreement with Stokes law. Stokes law is used to determine the settling velocity of smaller particles. For  $D_{\text{s}} < 64\mu\text{m}$ , a fixed settling velocity is defined. For this study a default value is used, which is derived from the Stokes equation.

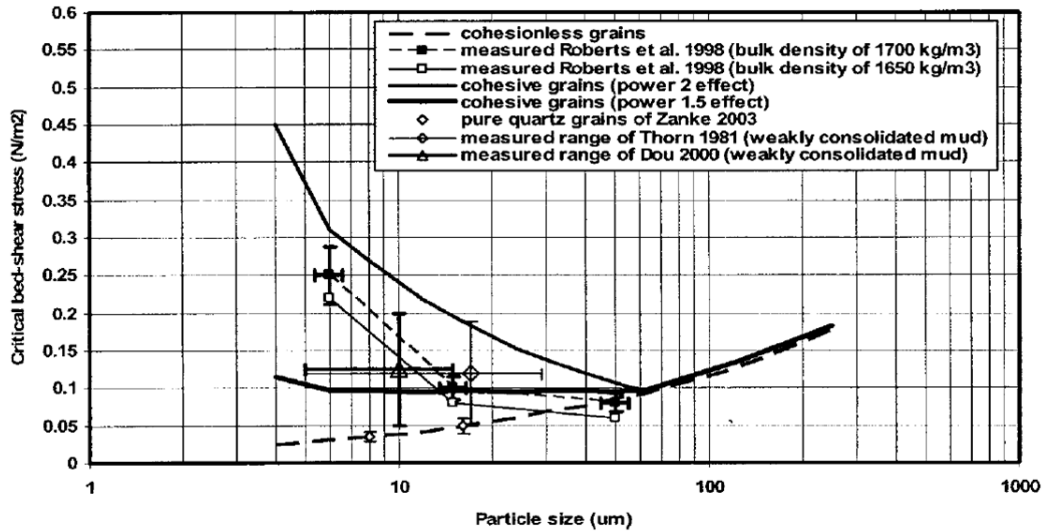


Figure 7: Effect of cohesive forces on critical bed shear stress of fine sediment beds. It is used as a guideline for picking representative critical bed shear stress values for the non-cohesive sediment classes ( $0 - 64\mu\text{m}$ ). From: van Rijn (2006)

## 2.3 Calibration

Calibration is a necessary and critical step to ensure that the model is representative. A heuristic method was used to find the most optimal set of input parameters. Preparatory to the large-scale simulations, earlier (small-scale) models were used as trial cases in order to find the right input values. In total 174 models have been tested of which only the final (MR) series are presented.

### 2.3.1 Splay Fine (SF) models

Firstly the effect of the bottom roughness, total discharge water-level ratio, morphological factor, and numerical momentum/transport schemes were tested in a coarse grid ( $100 \times 100$ ) with only 3 flooding cycles. The output from the SF-series (SF1-25)<sup>2</sup> resulted in the following conclusions:

- For stable runs the explicit flooding scheme is needed. However, this leads to a time step condition to ensure numerical stability (eq. 1).
- A morphological factor between 10 and 20 gives an optimal result. During the evaporation stage a higher morphological factor of 60 is needed to account for the slow settling of fines, whilst keeping simulation time to a minimum.
- A morphological factor of 60 during the evaporation stage gives unstable situations at the inflow boundary. This is caused by a too high sedimentation rate, which leads to numerical instabilities. This is solved by setting the inflow of sediment to zero during the evaporation stage.
- The distinct crevasse formation and inundation stages only occur for given discharge (B.C.1) and water level (B.C.2) values.
- For bottom roughness the manning correlation with a manning coefficient of 0.03 gives the best result

<sup>2</sup>See Appendix B

- The critical shear stress for erosion should be set higher than the literature values. Otherwise unrealistic incision depths are reached.

$$\Delta t \leq \frac{1}{D_H} \left( \frac{1}{\Delta x^2} + \frac{1}{\Delta y^2} \right)^{-1} \quad (1)$$

In which  $\Delta t$  : Maximum time step [s],

$D_H$  : Horizontal eddy diffusivity [ $\text{m}^2\text{s}^{-1}$ ],

$\Delta x, \Delta y$  : The grid dimension in x and y direction [m]

### 2.3.2 Multi Run (MR) models

The second step was simulating nine cycles on a 200x200 grid. For these models bathymetry 1 & 3 was used as initial model. The goal of this series was to study the effect of sediment input and the composition of the substrate. The corresponding sediment properties were kept constant for the simulations (table. 3). The models of the MR series were further analysed and their results are presented in the result section.

| Median Grain size | $v_{\text{sed}}$    | $\tau_{\text{cr,b,sed}}$ | $\tau_{\text{cr,b,ero}}$ | $\rho_{\text{set}}$ | $\rho_{\text{spec}}$ | $C_{\text{ero}}$  |
|-------------------|---------------------|--------------------------|--------------------------|---------------------|----------------------|-------------------|
| 7                 | $3.2 \cdot 10^{-5}$ | 1000                     | 1                        | 1600                | 2650                 | $1 \cdot 10^{-4}$ |
| 25                | $1.0 \cdot 10^{-3}$ | 1000                     | 0.5                      | 1600                | 2650                 | $1 \cdot 10^{-4}$ |
| 45                | $5.0 \cdot 10^{-3}$ | 1000                     | 0.3                      | 1600                | 2650                 | $1 \cdot 10^{-4}$ |
| 64                | -                   | -                        | -                        | 1600                | 2650                 | $1 \cdot 10^{-4}$ |
| 80                | -                   | -                        | -                        | 1600                | 2650                 | $1 \cdot 10^{-4}$ |
| 110               | -                   | -                        | -                        | 1600                | 2650                 | $1 \cdot 10^{-4}$ |

Table 3: Sediment properties used for the MR models

### 2.3.3 Splay Big (SB) models

The last step was to perform simulations with bathymetry 2 as the initial bathymetry. The output was not further analysed, as it was not representative for the Río Colorado fluvial system<sup>3</sup>.

## 2.4 Data Processing

Delft3D outputs hydrodynamical, morphological and sedimentary data for every pre-defined time step. However, the format of sediment output is not comparable with the field data. The model works with a small amount of discrete sediment classes ( $n < 10^1$ ), whereas the sediment distributions measured with a laser diffraction spectrometer (Bürkholz and Polke, 1984), approximate a continuous distribution ( $n > 10^2$  classes). Therefore, an integrated statistical approach was used to transform the models output into usable distributions. First, field data were analysed in a genetically meaningful way (Weltje and Prins, 2007). Subsequently, this analysis was applied on the discrete model output to derive comparable grain-size distributions.

<sup>3</sup>See Appendix F

| Splay Name | Latitude     | Longitude    | Sampled in: |
|------------|--------------|--------------|-------------|
| CS-1       | -20.49855212 | -66.96164738 | 2013 & 2014 |
| CS-2       | -20.53162550 | -66.94604982 | 2013 & 2014 |
| CS-24      | -20.58400172 | -66.86700912 | 2014        |

Table 4: Table showing the location of analysed crevasse splays



Figure 8: Example of a crevasse splay (CS-2) situated in the Río Colorado fan. It has been visited during the two campaigns and the sediment sample pit locations are depicted by the markers.

#### 2.4.1 Field data analysis

Data was gathered in two field campaigns. The first aimed to characterize the sediment distribution within a crevasse splay and construct a static model (Torres Carranza, 2013). The second is part of ongoing research and dates from 2014 (table 4). It was designed to quantify the effect of the distance sediment travels within and out of a crevasse channel (fig. 8). The data show that sediment in a crevasse splay often comprises two main fractions. The coarser fraction is associated with deposition in a waning flow regime, whereas the finer fraction precipitated during floodplain inundation. Therefore, the distributions were decomposed in two separate fractions, representing these two different depositional mechanisms.

Fitting exercises show that a Weibull function yields the best fitting results for fluvial sediments. This implies that fluvial grain-size distributions can be approximated by the summation of two weighted Weibull functions (Sun et al., 2002):

$$f(x) = c \left[ \frac{k_1}{\lambda_1^{k_1}} (x)^{k_1-1} e^{-\left(\frac{x}{\lambda_1}\right)^{k_1}} \right] + d \left[ \frac{k_2}{\lambda_2^{k_2}} (x)^{k_2-1} e^{-\left(\frac{x}{\lambda_2}\right)^{k_2}} \right] \quad (2)$$

In which  $f(x)$  : Probability density function,  
 $k, \lambda$  : Weibull constants,  
 $c, d$  : Scalars of the two elemental Weibull distributions.

A least-square fitting method was used to derive the parameters  $c, d, \lambda_1, \lambda_2, k_1, k_2$  for every sediment sample. The result is two separate fractions per sample, each described by a continuous distribution (fig. 9) with a corresponding median ( $\mu$ ) and standard deviation ( $\sigma$ ).

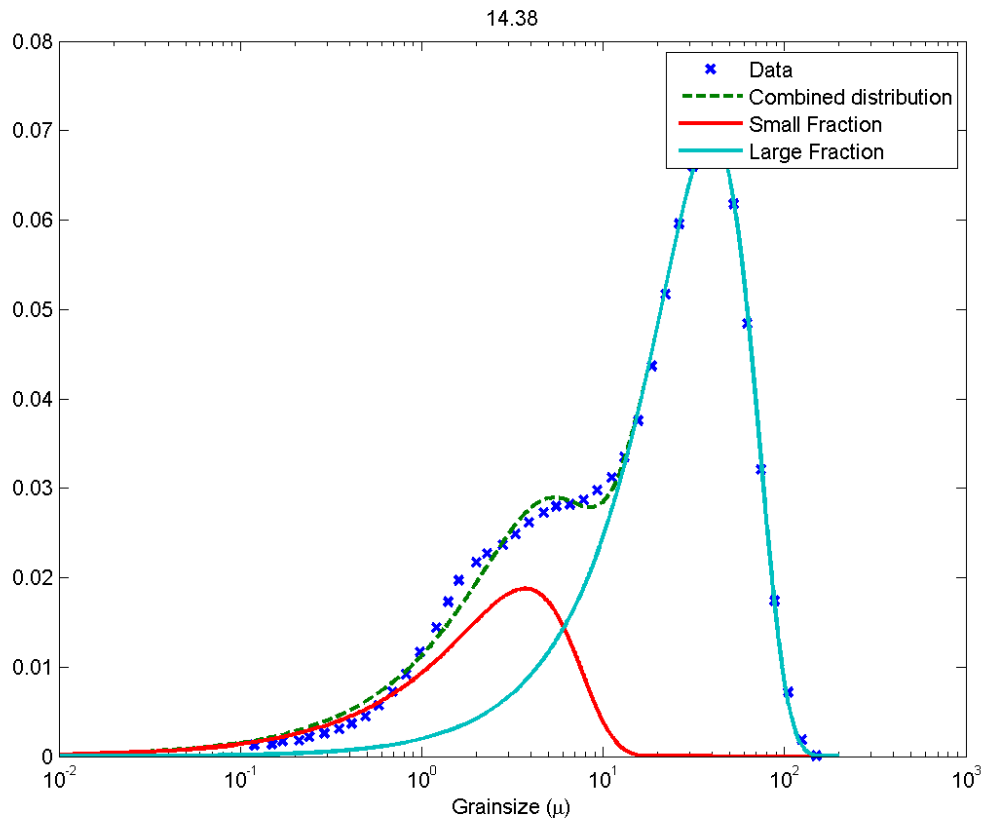


Figure 9: Field data from sample 14.38 and corresponding probability density functions.

**Distance in and out of crevasse channel** Torres Carranza (2013) posed the hypothesis that distance in and out of the crevasse channel are the most significant controls for grain-size distribution. This is in line with the general understanding that sediment deposition is correlated with flow energy. An analysis was performed on the available field data linking the distance in and out of the crevasse channel, with the grain-size data. The spatial relation between the geo-referenced sample pits and crevasse channels was determined by using satellite images of the sampled crevasse splays (fig.8). An algorithm calculated the shortest distance from the sample point to the crevasse channel by determining the orthogonal path towards the crevasse channel. The path the sediment travelled within in the crevasse channel is calculated by determining the combined length of crevasse channel between projected point and the levee breach (fig.10). This analysis has been carried out for three different crevasse splays.

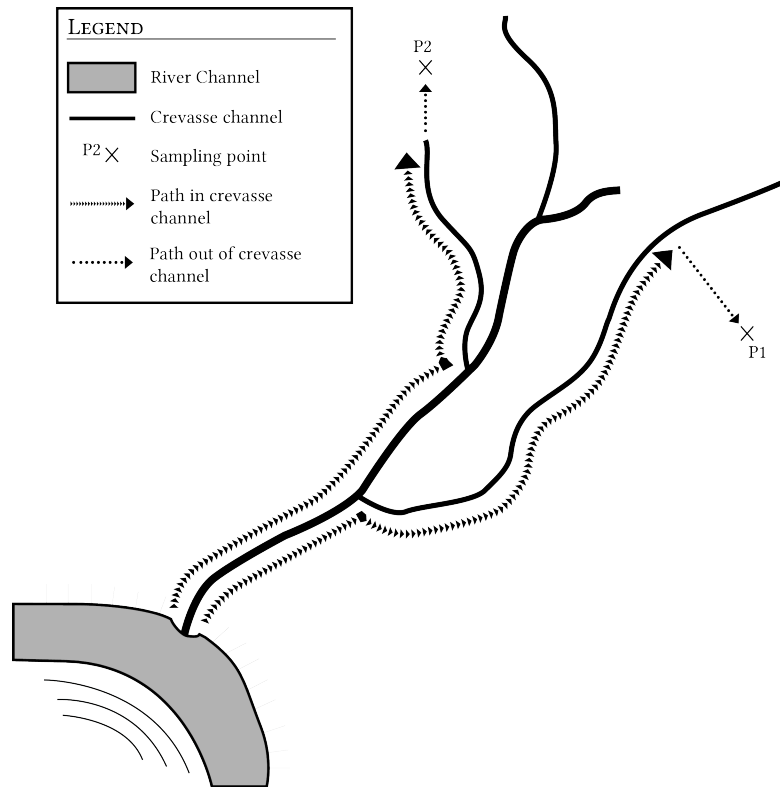


Figure 10: The distance sediment from two samples (p1 & p2) traveled in and out of the crevasse channel.

#### 2.4.2 Model data analysis

The model output consists of few discrete grain-size classes. In order to process it the same way as the field data, two assumptions were made:

1. The discrete grain-size classes are  $n$  samples from a continuous grain-size distribution.
2. For  $n \rightarrow \infty$  the down-sampled data converge to the true grain-size distribution.

These two assumptions result in the following workflow: The discrete grain-size classes are represented in a cumulative distribution plot. Two Weibull distributions are fitted, resulting in two Weibull functions (fig. 11). This work flow is repeated for a selection of grid-cells and assigns each its grain-size parameters including the median and standard deviation.

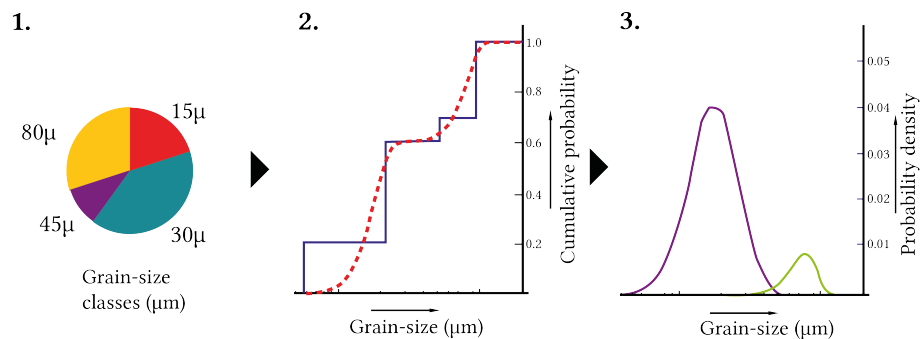


Figure 11: The workflow for deriving continuous distributions from discrete model output.

### 2.4.3 Statistical error

A study was performed on the effect of using a limited amount of grain-size classes. It consists of a routine that downsamples the grain-size data from the Uyuni field campaign (2014). The probability of a sample  $n$  is calculated by averaging the  $i$  number of data points that are included in the  $x$  domain of bin  $n$  :

$$p_{n,\text{sampled}} = \left( \frac{1}{2}x_{(n+1)} - 2x_n + \frac{1}{2}x_{(n-1)} \right)^{-1} \cdot \sum_{i=1}^{n,i} p(x_{n,i}) \cdot \Delta x_{n,i} \quad (3)$$

In which  $p_{n,\text{sampled}}$  : Probability density of downsampled bin  $n$

$x_{(n)}$  :  $x$  value of bin  $n$ ,

$p(x_{n,i})$  : Probability density of data point  $i$  in the domain of bin  $n$ .

$\Delta x_{n,i}$  : The  $x$ -width of data point  $i$  in the domain of bin  $n$ .

Subsequently, the fitting routine used for the raw data was performed on this downsampled data. The resulting distributions were compared with distributions that were fitted to the full data set, i.e. the relative error of the mean for sample  $n$  is the absolute difference between the both means divided by the 'real' mean. The average relative error of all samples was compared for different amounts of bins used for the downsampling.

### 2.4.4 Derivation of Porosity and Permeability

**Porosity** Particle size distribution greatly effects the porosity of a sediment pack. Several models exist in literature that try to link these two sediment properties (Ouchiyama and Tanaka, 1989). In this research, two different models are used. The first model is an analytic linear-mixture packing model proposed by Yu and Standish (1991). It includes the (un)mixing effect (fig. 12) which results in a correlation between the 'size ratio' and 'fraction of solid volume of large particles' of binary discrete mixtures to porosity (fig. 13).

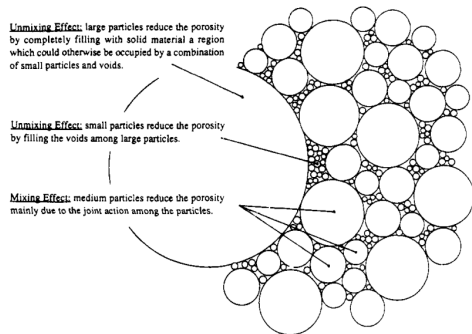


Figure 12: Two-dimensional diagram illustrating the random packing structure of spheres from: Yu and Standish (1991)

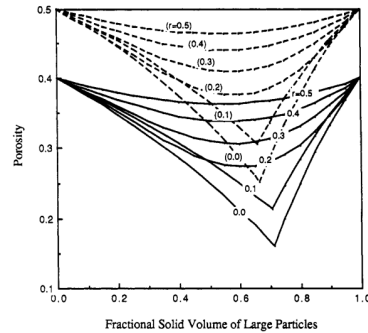


Figure 13: Calculated porosity of binary mixtures from: Yu and Standish (1991)

A major weakness of this method is the fact that real sediments are best described by continuous distributions. Yu and Standish (1993) show that the the results of discrete distributions cannot simply be extrapolated. The results are a more qualitative approximation of porosity, so a form of calibration is essential.

The second method comprises an empirical correlation between the standard deviation ( $\sigma$ ) of the distributions and the porosity ( $\phi$ ) (eq.4). It is based on field observations performed by Takebayashi & Fujita in 2014.

$$\phi = 0.38 \cdot \frac{3.7632\sigma^{-0.7552}}{1 + 3.7632\sigma^{-0.7552}} \quad (4)$$

The in-situ porosity is estimated based on its relationship to mechanical compaction. Bahr et al. (2001) proposed a simple exponential relation with depth ( $z$ ) (eq. 5), with a compaction coefficient  $\beta$  ranging between  $2.7 \cdot 10^{-4}$  and  $15.5 \cdot 10^{-4}$ .

$$\phi = \phi_0 \cdot e^{(-\beta \cdot z)} \quad (5)$$

**Permeability** The permeability is determined with a modified Carman-Kozeny formula, which includes the information on grain-size distribution (Panda and Lake, 1994). The permeability is calculated with the porosity and the first three statistical moments as input (eq.6).

$$k = \frac{\overline{D_p^2} \phi^3}{72\tau(1-\phi)^2} \left[ \frac{\left( \gamma \left( \frac{\sigma}{\overline{D_p^2}} \right)^3 + 3 \left( \frac{\sigma}{\overline{D_p^2}} \right)^2 + 1 \right)^2}{\left( 1 + \left( \frac{\sigma}{\overline{D_p^2}} \right)^2 \right)^2} \right] \quad (6)$$

In which  $k$  = Permeability [ $\text{m}^2$ ],

$\tau$  = Tortuosity [-],

$\overline{D_p^2}$  = Mean grain size diameter [m],

$\phi$  = porosity [-],

$\sigma$  = Standard deviation of grain-size distribution [-],

$\gamma$  = Skewness of grain-size distribution [-]

### 3 Results

The results of the runs are presented for initial bathymetry 1 and 3. The second part consists of the field data analysis results and the consequent error and sensitivity analysis.

#### 3.1 Bathymetry 1

In this section the results from model MR-1, MR-2, and MR-3 are presented.

**Morphology** The model shows a steady increase of the water level within the river channel. At a critical water level, the levee is breached leading to the erosion of the levee at the breach point. Through this gap, a concentrated flux of water travelling with a velocity of up to 1 m/s enters the floodplain. The result is a 70 m long incision with a maximum depth of 40 cm at the breach point. Beside these incisions, small levees are formed beyond which the finer sediments are deposited. At the downstream end of the incision, the bedload settles and forms a mouth bar (fig. 14).

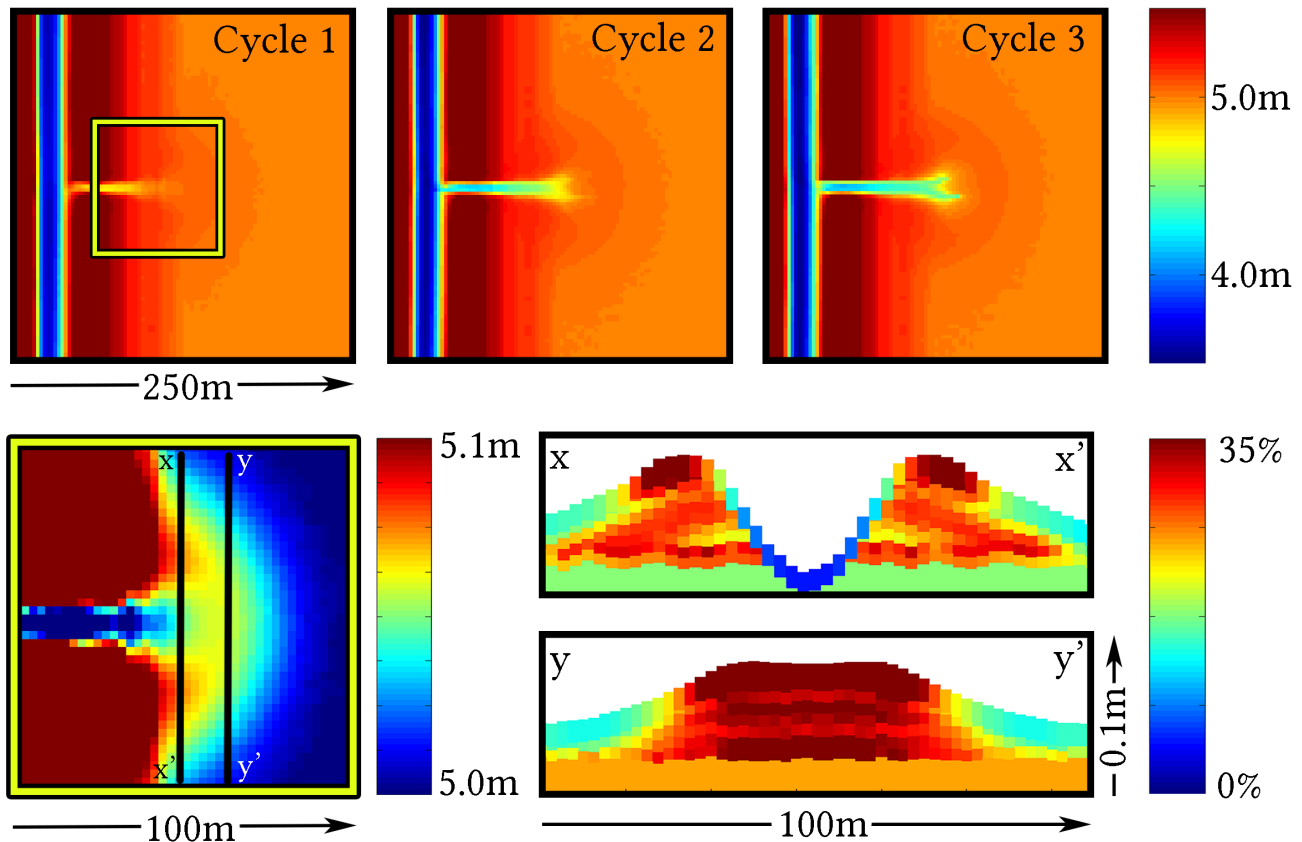


Figure 14: The bathymetry of model MR-2 after 1, 2 and 3 consecutive flooding cycles. In the yellow box an close up is shown with a different scale in order to emphasize the levee and mouth-bar structures. In cross section  $x-x'$  the small crevasse-channel levees and incision are represented. In cross section  $y-y'$  the coarse grained accumulation is shown, which is interpreted as a mouth bar. The colours in the cross sections represent the volume fraction of the largest grain-size class.

The channelized flow onto the floodplain evolves in a sheet flood as soon as the discharge through the levee breach exceeds the capacity of the crevasse-channel. This leads to the complete inundation of the floodplain with a maximum water depth of 15 cm. The flooding stops when the river water level falls below the crevasse-channel floor at the levee breach. The result is two non-communicating water bodies. One is the confined flow within the river channel and the other is a stagnant sheet of water on the inundated floodplain. Subsequently, the latter water body slowly disappears through evaporation and absence of any water supply.

Consecutive flooding events result in the further erosion and, hence, the further development of the crevasse-channel system. In Cycle 2, the levee breach is excavated to such a depth that part of the water from the inundated floodplain can flow back into the river channel. This reflux of floodplain water causes erosion at the point where the water re-enters crevasse-channels (fig.15). This stage shows highest bed-load transport rates within the crevasse-channel (fig.16). In Cycle 3, the mouth bar reaches a critical mass resulting in a bifurcation (fig. 14).

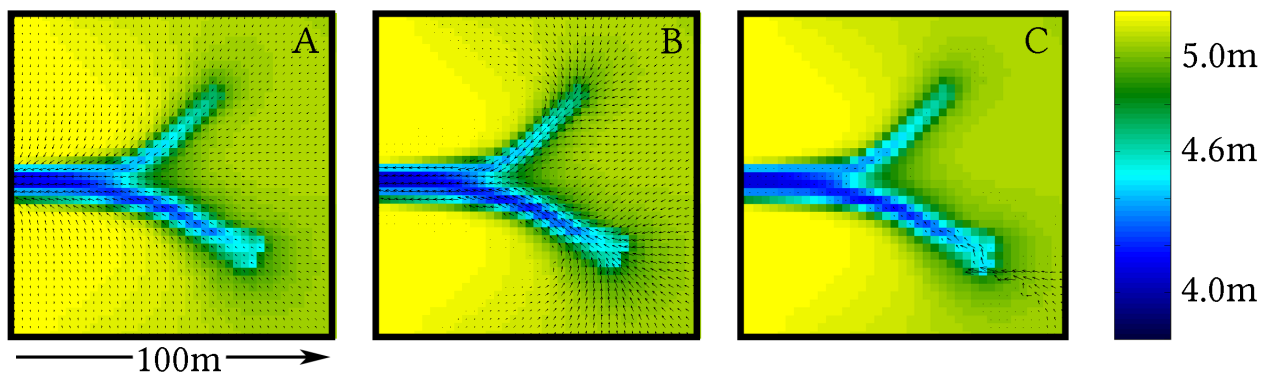


Figure 15: The reflux of water into the crevasse-channel system. The colours represent the bed level. The arrows represent the relative water velocity. A) The first stage of reflux after the full inundation of the floodplain. B) The intermediate stage of reflux. The water evades the highs created by sediment deposition and water enters at the distal part of the crevasse channel. C) Late stage of reflux. The water only enters the southern crevasse channel.

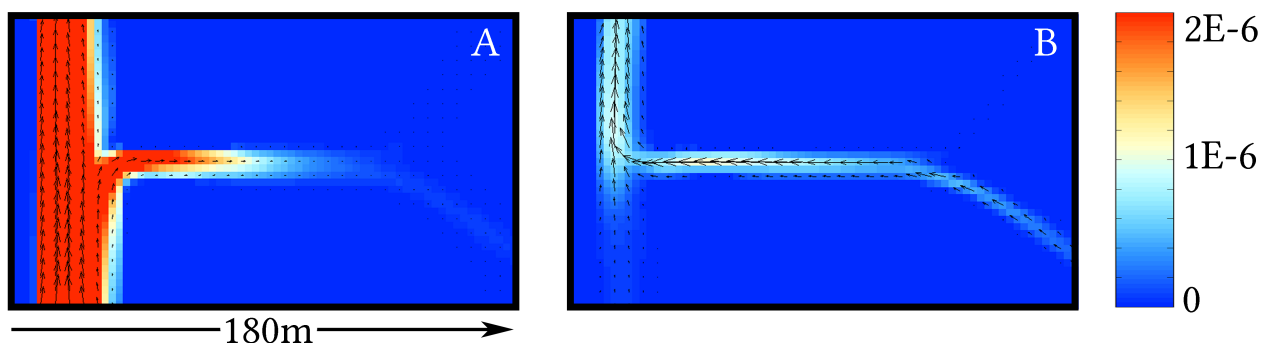


Figure 16: Bed-load transport at the river channel/ crevasse channel junction during A) Crevasse formation B) Reflux. The vectors represent the direction and relative magnitude of the transport. The colour represent the absolute magnitude in  $m^3 s^{-1} m^{-1}$ .

The final bathymetry after nine cycles consists of a simple crevasse channel system with one bifurcation at most (fig. 17). Close to the levee breach, the main crevasse channel is 15m wide and 90 cm deep. The crevasse channels cross-sectional area decreases in more distal sections.

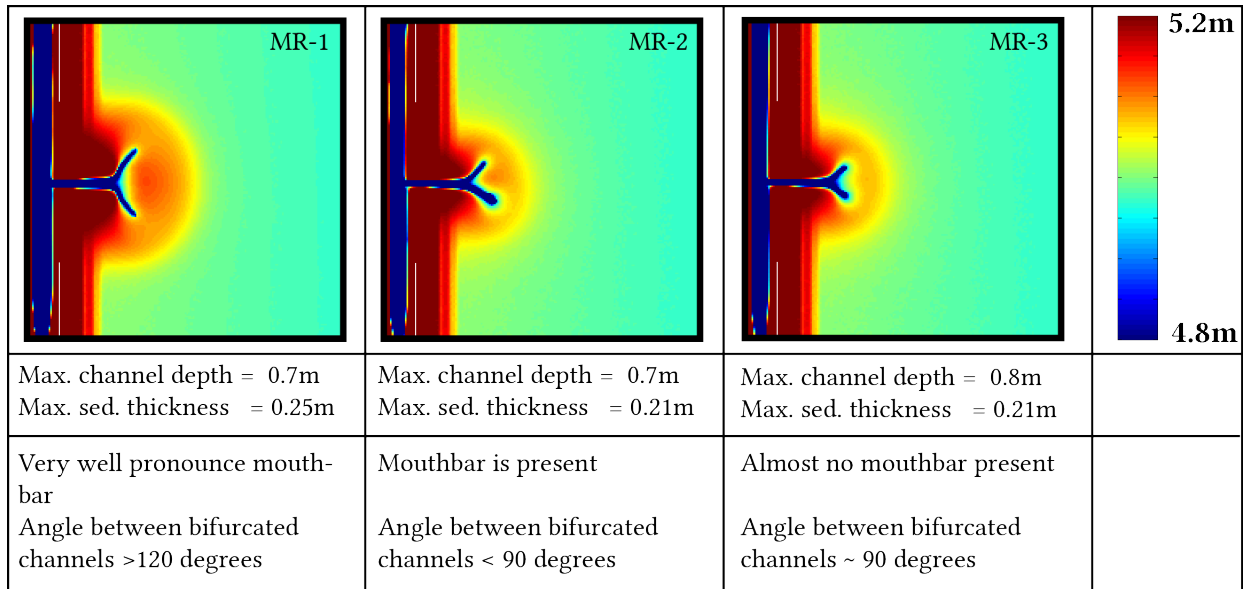


Figure 17: MR-1 uses sediment set 1  $\mu\text{m}$ . MR-2 sediment set 2  $\mu\text{m}$ . MR-3 uses sediment set 3. All three models have seen nine flooding cycles.

At the crevasse/river junction sediment bars are formed due to reflux of water and sediment from the floodplain into the river channel when the discharge decreases (fig. 18). The morphology of these reflux bars are different for the different sediment sets. The coarser sediment set (MR-1) shows a pronounced elongated bar downstream of the junction, where the upstream bar is almost absent. The smaller sediment set shows a less elongated bar downstream of the junction where the upstream bar is well pronounced. During the confined flow stage, parts of these bars closest to the river channel axis are eroded and transported further down river. The upstream bar, when it is well pronounced, is subject to the highest rates of erosion. The upstream bar is almost absent within two hours.

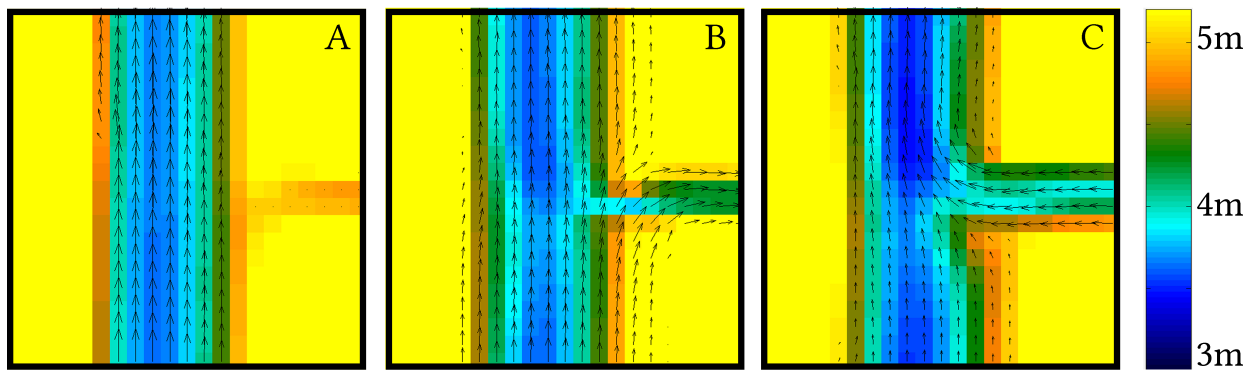


Figure 18: Morphology and fluid flow in model MR-2 at the levee breach. The colours illustrate the bed level in meters and the vectors represent the flow direction and relative magnitude. The displayed domain comprises 50 x 50m. A) Shows the confined flow before breaching the levee. B) Shows the levee breach and water flowing towards the floodplain. Sediment is deposited in the river channel downstream from the crevasse-channel/river-channel junction. C) Shows the reflux of water from the floodplain into the river channel. Note that bars are being formed both up- and downstream of the crevasse channel.

On the floodplain an accumulation of sediment is present which shows an exponential thinning trend away from the crevasse channels. The sediment accumulation on the floodplain measures 100-150m perpendicular

to the river channel, 200-300m parallel to the river channel and 5-25 cm in thickness.

The further behaviour of crevasse splays has only been studied for model MR-2 (fig 17B). After nine cycles, the discharge trough the northernmost branch starts to decrease, which leads to the complete dominance of the southern crevasse channel after 12 cycles. The result is an asymmetric crevasse splay with dimensions of 150m x 200m.

**Sedimentary trends** The proximal part of the crevasse splay mainly consists of the medium to coarse silt fractions (Appendix E b&c). Meanwhile, the volume fraction of the smallest grain-size class increases with distance from the crevasse channel (Appendix E d). The volume fraction and median grain size of the large fraction show an overall fining trend proximal to distal from crevasse channel. This results in higher permeability values for locations close to the apex and/or a crevasse channel (fig. 19 & 20).

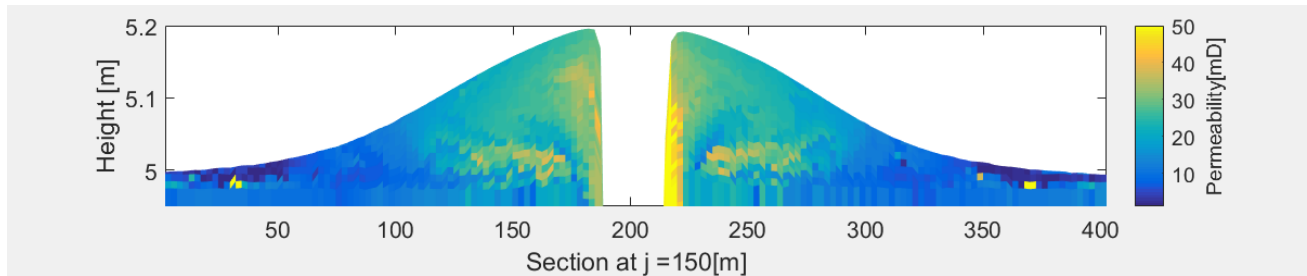


Figure 19: Cross section at  $j = 150\text{m}$ . It displays the highest permeability values in mili Darcy; situated close to the crevasse channel. Note that the permeability rapidly decreases towards the edges of the crevasse-splay.

Cross sections through the crevasse splays show an overall fining upward trend. On a 2-5 cm scale, two to three fining upward zones can be distinguished (fig. 21). Analysis of these cross section through time shows that this layering is the result of different flooding cycles. The architecture of the layering is dependent on the local ratio between the erosion and deposition during the 'crevasse formation' and 'reflux stage'.

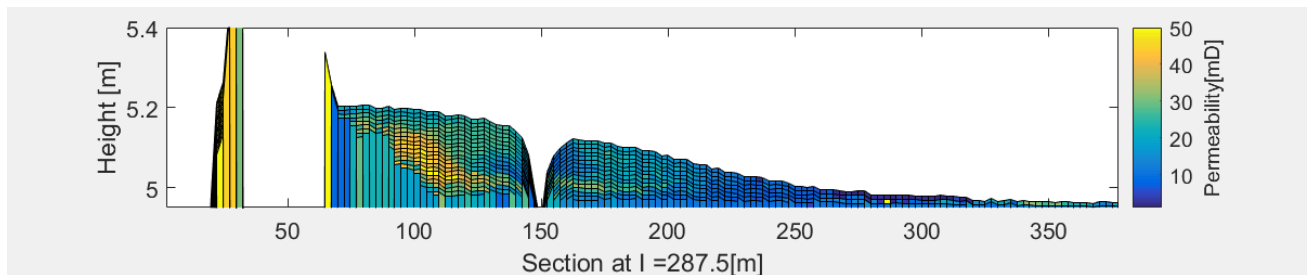


Figure 20: Cross section at  $i = 287.5\text{m}$ . It shows the permeability relation perpendicular on the river channel.

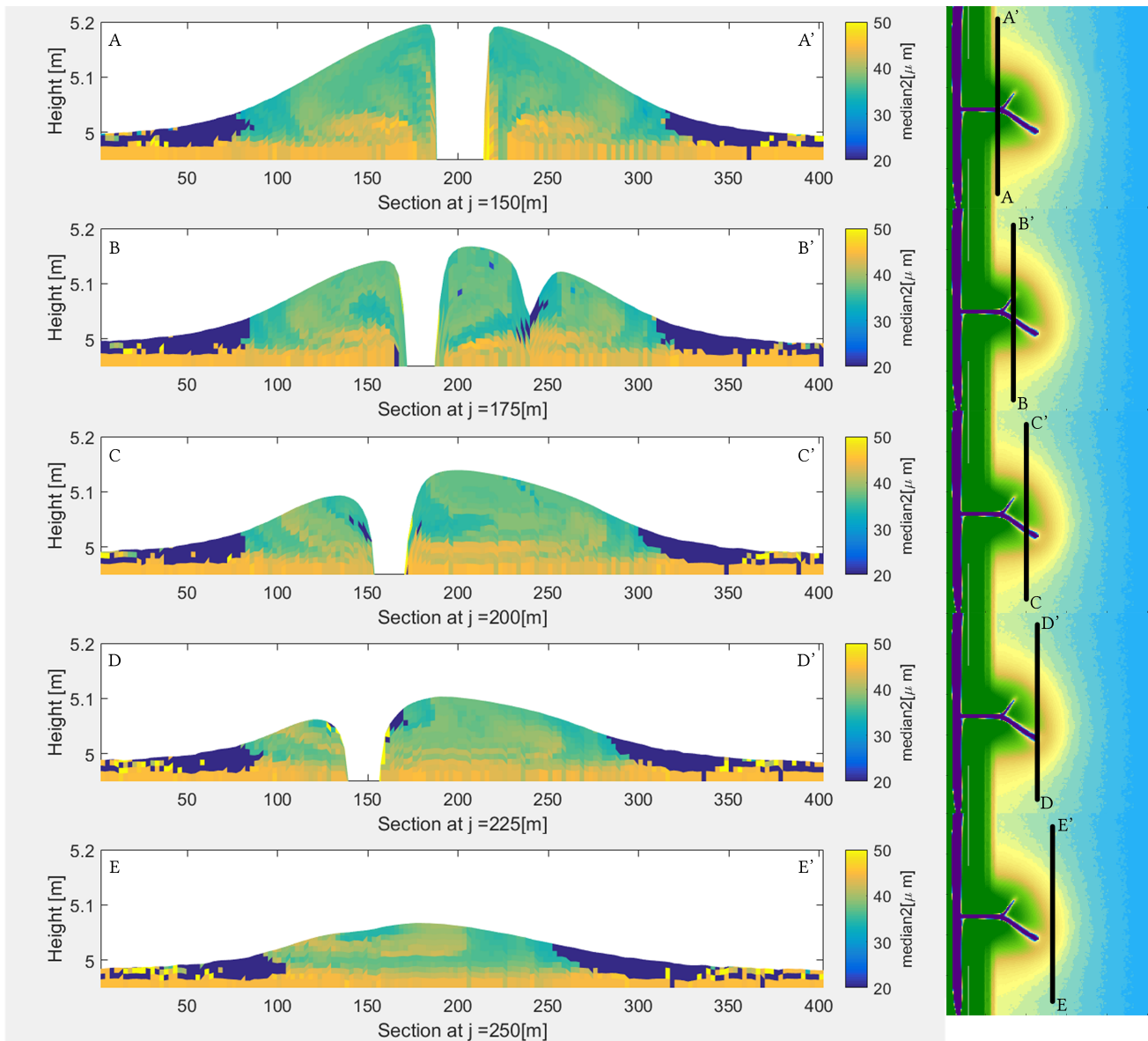


Figure 21: Cross sections through the resulting sediments after 18 cycles. The colours illustrate the median of the large grain-size fraction.

When taking a closer look at the values at 10cm depth below in the crevasse splay we can see that sediment trends are better visible for a combined mean. For a more proximal cross section the large fraction shows a more or less constant grain size with a steep decline at 270 meter from the crevasse channel (fig. 22 A). The total mean on the other hand shows an roughly parabolic decline (fig. 22 B). For a more distal cross section the large fraction shows a more irregular behaviour. The total mean shows a similar trend as its counterpart but with smaller grain sizes (fig. 22 C&D).

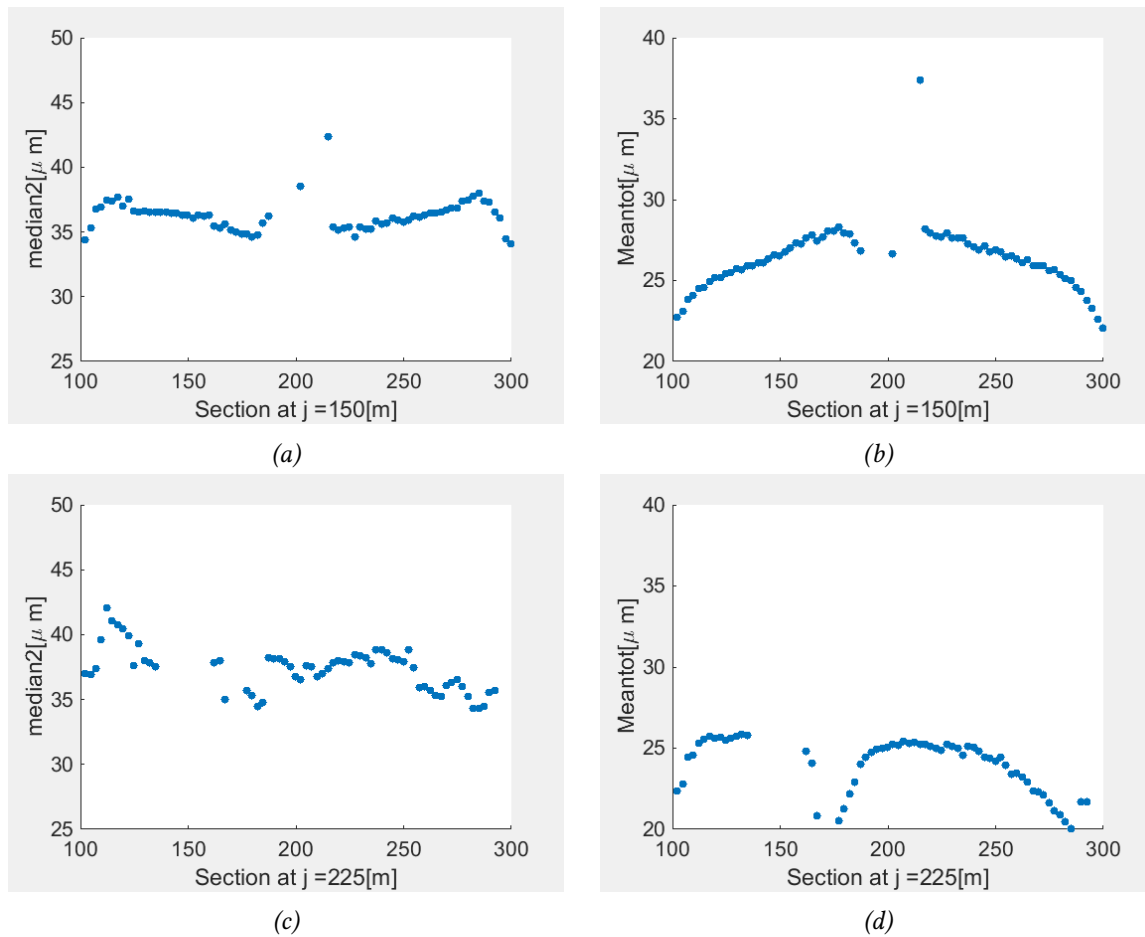


Figure 22: The total mean shows clearer sedimentary trends. (a) & (b) are the total and median of the large fraction of cross section A-A' from figure 21. (c) & (d) shows the same but then from cross section D-D'

### 3.2 Bathymetry 3

In this section the results from models MR-2COMP-1, and MR-2COMP-2 are presented. The lateral spacing between the central axis of the predating crevasse-plays in MR-COMP-1 and MRCOMP-2 is 250m and 350m respectively (fig.23 & 25).

**Morphology** After 9 cycles MR-2COMP-1/2 show a sediment accumulation on the topographic low between the two initial crevasse splays (fig. 23). The deposit directly aggrades/progrades in contradiction to the incisive behaviour observed for bathymetry 1 & 2. MR-2COMP-1 shows that after 12 cycles the crevasse channel incisive through the confinement (fig. 24). This opens the gate towards the more distal floodplain for coarser material.

**Sedimentary trends** The sedimentology for the aggrading simulations is correlated with the pre-dated crevasse splays. They create a confinement between them, given that they are situated close enough to each other. In this confinement relative coarse sediment is being deposited. Most of the finer sediment is transported more distally onto the floodplain. This results in contact between the 'coarser' proximal parts of the crevasse splays (fig. 23). This contact is lost for the more distal parts where the nesting crevasse splay contains predominantly fines. This higher permeability zone is not present in model MR-2COMP-2 cross-sections (fig. 25). A band of fine sediment is present on the contact between the pre-dating and nesting crevasse splays.

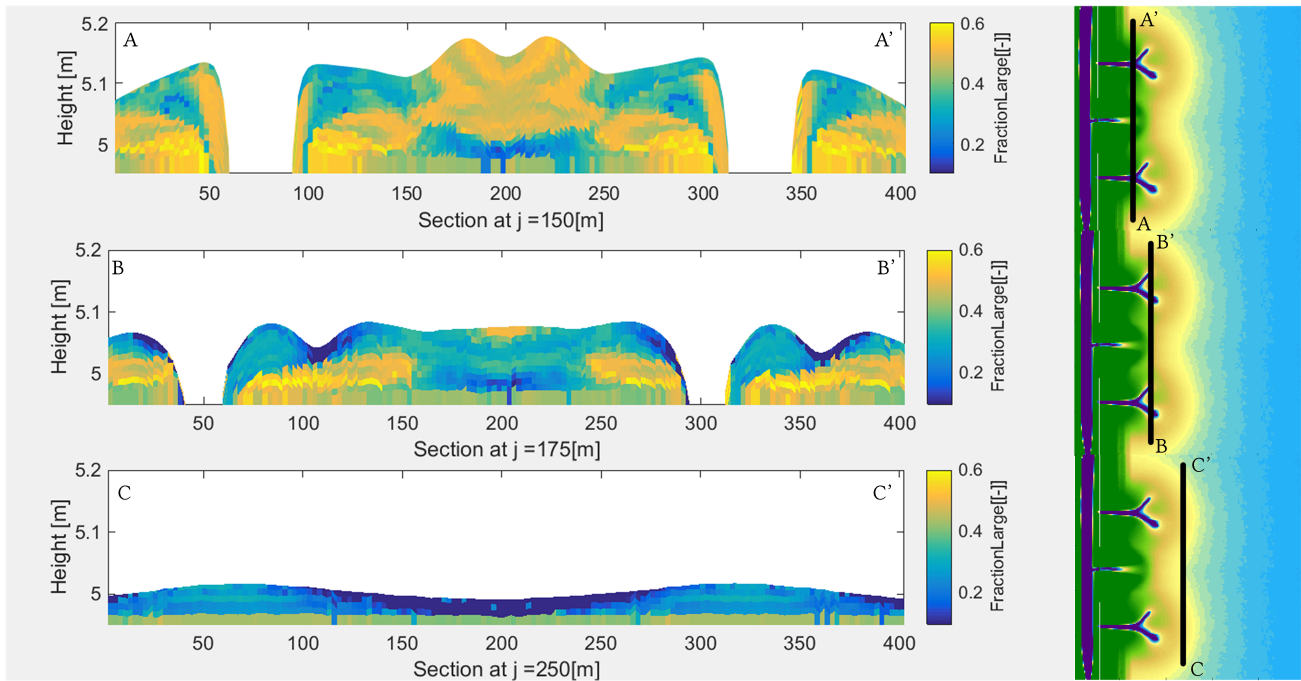


Figure 23: Cross sections of model MR-2COMP-1 after 9 cycles showing the fraction of the large fraction.

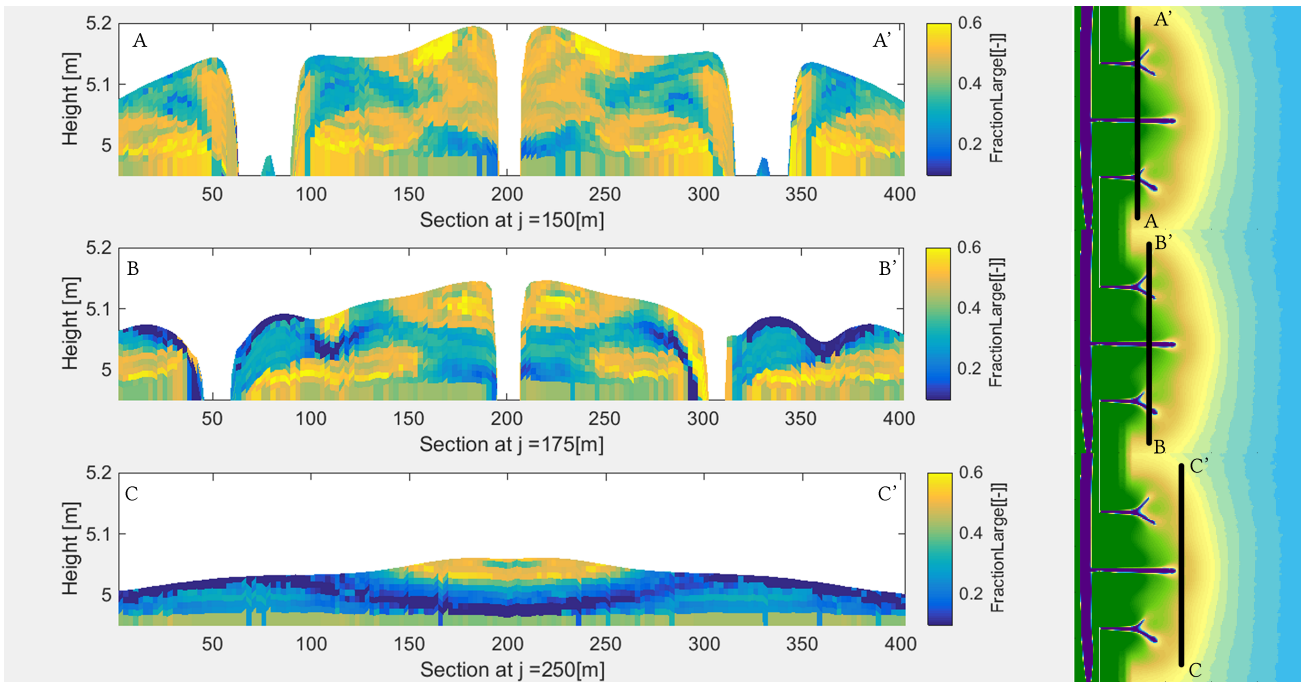


Figure 24: Cross sections of model MR-2COMP-1 after 18 cycles showing the fraction of the large fraction.

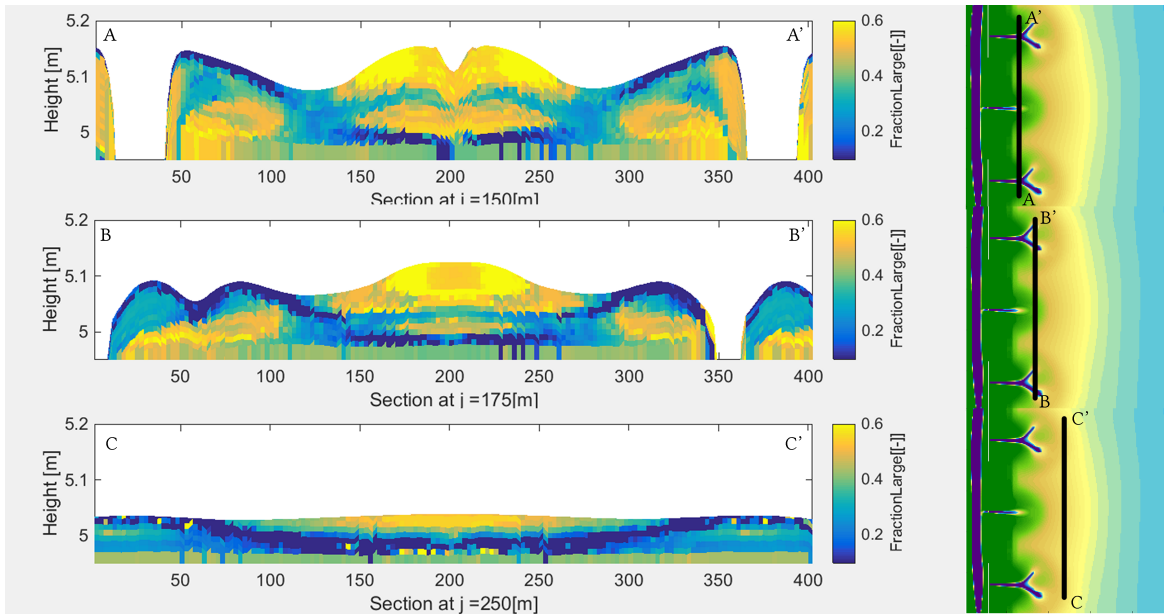


Figure 25: A cross section of model MR-2COMP-2. Note the higher fine fraction content at the contact between the nesting and predating crevasse-splays.

### 3.3 Statistical Error & Sensitivity

Lumping data in a smaller amount of bins directly has an effect on the goodness of fit. Two types of fitting errors can be distinguished. The first is related to the positioning of the bins. For certain grain-size samples, using a small amount of bins fails in offering a correct anchorage for the fitting routine. This leads to a wrong estimation of one or both of the components statistical distributions. Consequently, it leads to 1-2 orders of magnitude under/over estimations of the mean and median (fig. 26).

The second is related to the amount of bins. Fitting errors caused by this type are mostly effecting the shape of the components distributions (fig. 27, 28 & 29). This results in a smaller error for the median and mean of the distribution. However, higher statistical moments like the standard deviation can still be heavily effected. These type two errors show an asymptotic inverse exponential relation with the amount of bins used (fig 30).

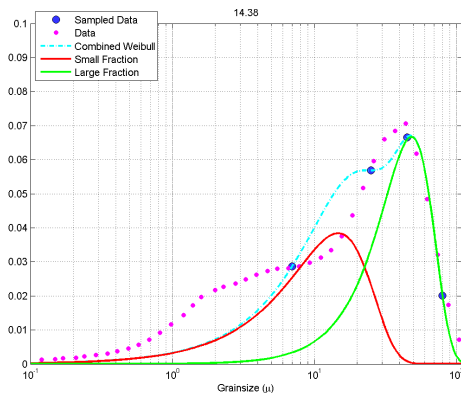


Figure 26: Grain - size data of sample 14.38 down sampled to 4 bins. Note the misfit which is caused by the absence of a data point in the smaller grain-size range.

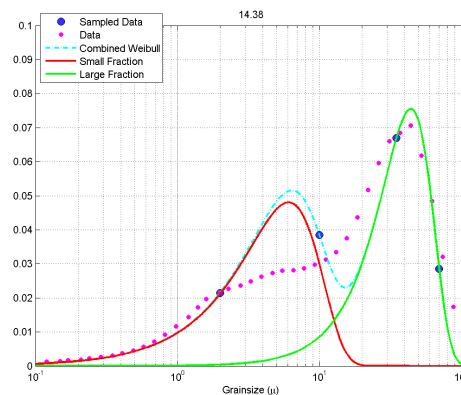


Figure 27: Grain - size data of sample 14.38 down sampled to 4 bins. The bins are chosen so that they result in a better fit in comparison with the bins in figure 26.

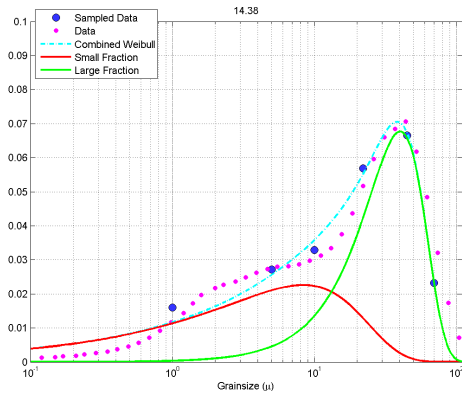


Figure 28: Grain - size data of sample 14.38 down sampled to 6 bins. It shows a better fit when comparing to figure 26 & 27

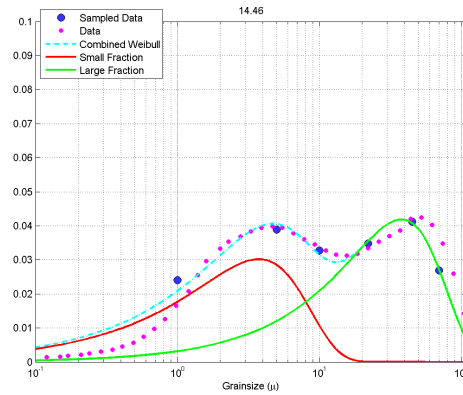


Figure 29: Grain - size data of sample 14.46 down sampled to 6 bins. It shows the applicability of the method to another grain-size sample.

### Av Relative Error Median Large Fraction

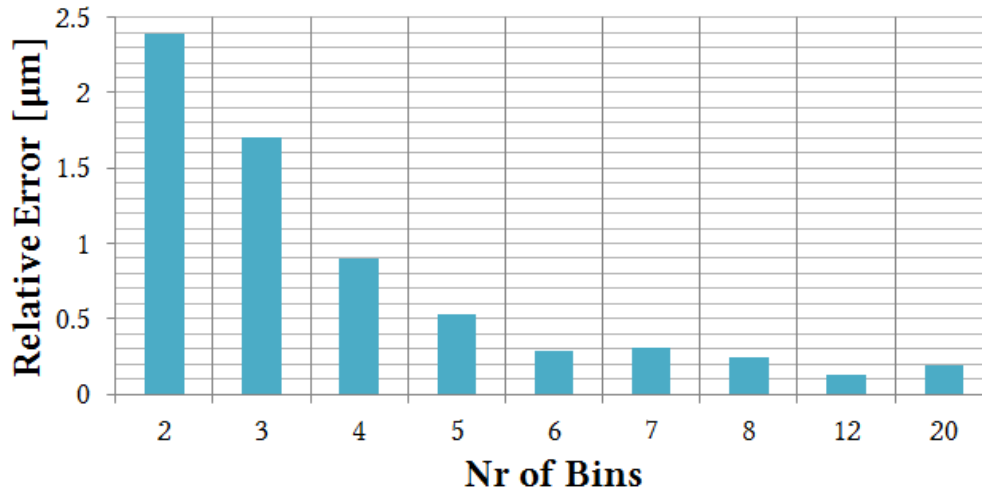


Figure 30: The average relative error for a increasing bin size.

### 3.4 Field-data analysis

**CS-1** The fitting routine of the field data results in good to very good fits ( $0.95 < R^2 < 0.99$ ). CS-1 shows a clear decrease in median grain-size of the large fraction for an increase in distance from the levee breach (fig. 32). The same trend can be observed for the average mean (fig. 31). Proximal (close to levee breach) samples show an inverse grain-size-distance-to-channel relation. This relation becomes less pronounced for more distal sample locations and in some cases it is even contradicted (e.g. at distance-in-channel = 800m). Overall, the median grain size of the large fraction is an inverse function of both distance-to/in-channel (fig. 33).

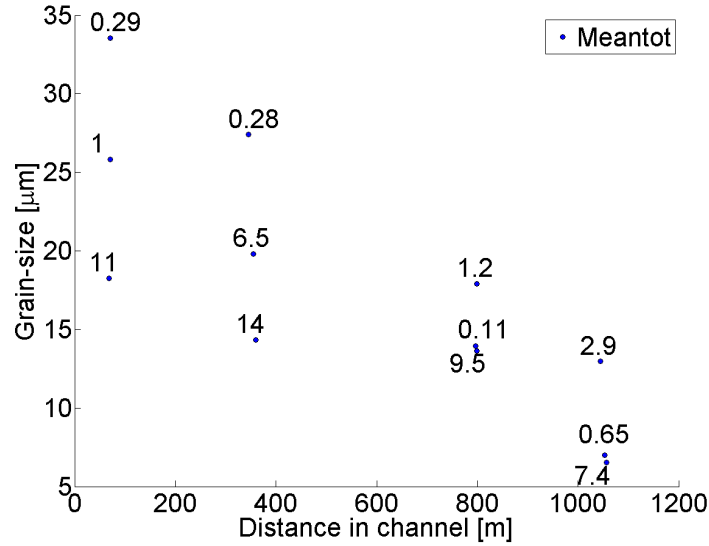


Figure 31: The averaged mean grain size (Meantot) plotted against distance in channel. The numbers displayed at the points represent the distance to the channel in meters. They displayed data was gathered during the second field campaign (2014). It originates from crevasse splay with code CS-1 and is filtered on depth = 10 cm.

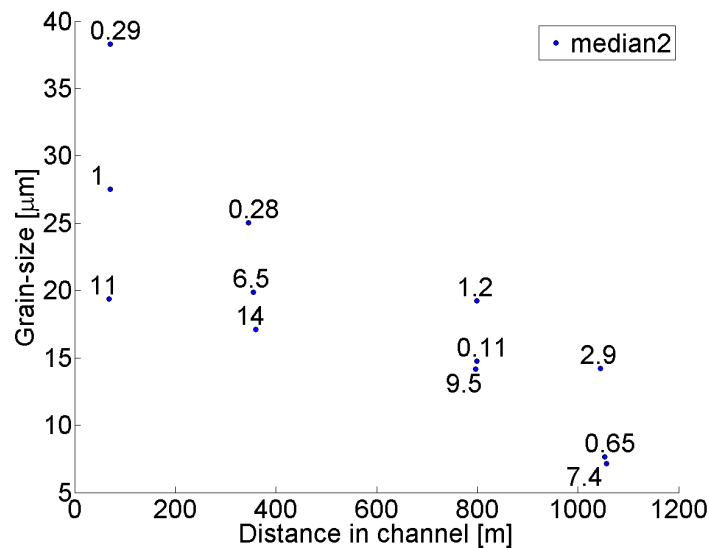


Figure 32: Grain-size plotted against distance in channel. The numbers displayed at the points represent the distance to the channel in meters. They displayed data was gathered during the second field campaign (2014). It originates from crevasse splay with code CS-1 and is filtered on depth = 10 cm. )

This relation is less clear in the data from the 2012 field campaign (Torres Carranza, 2013). The largest grain sizes ( $\pm 100\mu\text{m}$ ) are situated at 1200m distance-in-channel. The area close to the origin of the plot shows a heterogeneous assembly with grain-sizes ranging from  $20\mu\text{m}$  to  $70\mu\text{m}$  (fig. 34). The smallest grain sizes are found for high values of distance in/to channel ( $10 - 20\mu\text{m}$ ).

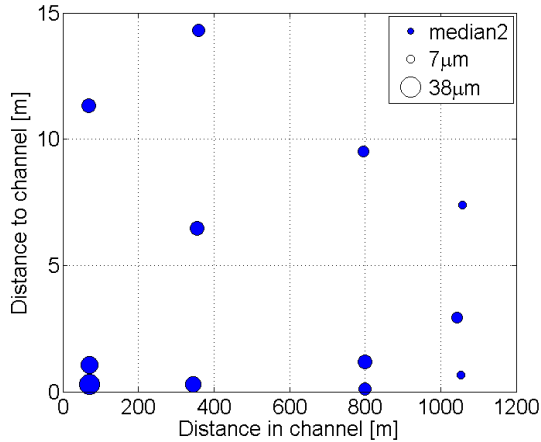


Figure 33: Grain-size distribution as function distance-to and distance-in channel. The displayed data originates from splay 1 and is gathered during the 2014 fieldwork.

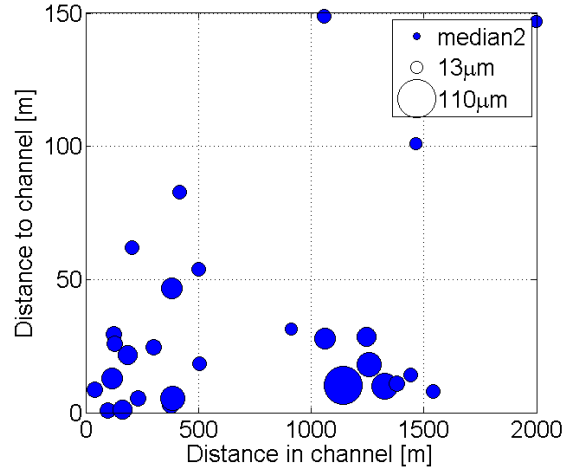


Figure 34: Grain-size distribution as function distance-to- and distance-in channel. The displayed data originates from splay 1 and is gathered during 2012 fieldwork (Torres Carranza, 2013).

**CS-2** Data from the 2014 field campaign on CS-2 doesn't show this inverse relation as strongly as CS-1. The strongest correlation is between grain-size and distance in channel (D-I-C). The more proximal samples (D-I-C  $\leq 600$  m) show grain sizes ranging from 15 to  $55\mu\text{m}$ . The more distal samples all show median grain-sizes smaller than  $16\mu\text{m}$ . Field data from the 2012 campaign also shows a more heterogeneous picture with a low correlation.

**CS-24** Data from the 2014 field campaign on CS-24 shows a inverse relationship with a good correlation between grain-size and distance-to/in-channel.

## 4 Discussion

A process-based model was developed and provides a physical view on the deposition of crevasse splays in four dimensions. The acquired insights can be used to improve the understanding of the different elemental morphodynamic processes and their effect on the resulting deposits. However, the models applicability is not self-evident, as it does not represent reality one-to-one. First the dynamic behaviour and governing forces will be discussed. Subsequently a link to the resulting morphology and sedimentary structures are made. As last, the validity of the estimated petrophysical parameters is discussed.

### 4.1 Crevasse splay dynamics

Fluvial systems, like any physical systems, strive to a state of minimum potential energy. Levee formation and aggradation can lead to an increased accommodation space on the floodplain (Dalman and Weltje, 2008). A potential difference is created when the water level exceeds the floodplain level. This potential difference ( $\Delta\Phi$ ) is the main driving force that governs the physical behaviour of overbank flow. A way to see the crevasse-splay system is a balance between driving and counteracting forces. The driving forces are a function of the  $\Delta\Phi$  and the distance between the points of the maximum and the minimum potential ( $\Delta L$ ): The hydrodynamical gradient ( $\frac{\Delta\Phi}{\Delta L}$ ) (fig. 35). This is counteracted by the frictional forces, who are a function of substrate composition, water velocity, hydraulic radius and fluid viscosity.

#### 4.1.1 Boundary conditions

Crevasse-splay formation is closely linked to the water level in the river. A confined flux of water is needed for a high velocity overbank flow (conservation of momentum). The result is a system with the potential to transport silt and fine sand onto the floodplain. The SF models show that a specific combination of hydrodynamical boundary conditions is necessary for the initiation of a crevasse splay. The water level should be high enough for a levee breach. However, it should not surpass the maximum levee height (fig. 35). This suggests that the presence and frequency of crevasse-splay formation is directly linked to the breaching proneness of the levees. Consequently, the levee height influences the maximum magnitude of the hydrodynamic potential difference, which has a direct influence on the crevasse splays morphology.

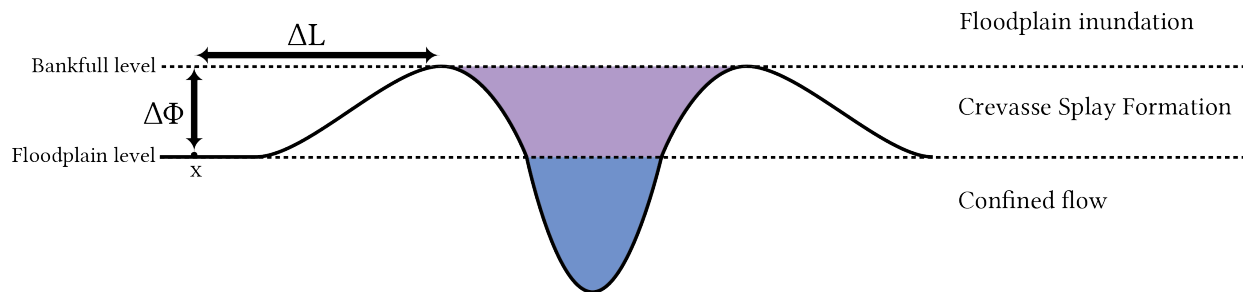


Figure 35: The possible response of the model for given ranges of water-levels. It also shows the potential difference which is a function of the levee height. The hydrodynamic gradient on the arbitrary point X is  $\frac{\Delta\Phi}{\Delta L}$ .

#### 4.1.2 Crevasse-splay evolution

The MR models show the distinct stages of a crevasse-splay life cycle. A crevasse splay is created when water finds its way through a local low in the levee. Hypotheses, how this low can be created, includes scouring

during overbank flow, and undercutting in a meander bend (Li and Bristow, 2015). During the initiation of a crevasse splay the rivers water level reaches almost bankfull. The hydrodynamical gradient between the adjacent floodplain and the top of the levee is higher than the hydrodynamical gradient of the river. This results in an acceleration of the water as it flows onto the floodplain. The increasing flow velocity promotes the transportation of sediment. The result is an under-saturated flow that starts to locally erode the levee and carves an increasingly deeper incision. At this point, flux is high enough to erode a crevasse-channel network that extends from the levee breach. Sediment is transported through this channel network onto the floodplain, where all of it is deposited.

The initial erosional behaviour has been observed during the early stages of a crevasse splay situated in the Mississippi Delta (Yuill et al., 2016). The observed morphology was used as an input for morphodynamic simulations using a 3D (not 2DH) version of Delft3D. The study shows similar elements observed in the MR models of this study (fig. 36). The deposition of this distinct architecture can be associated with turbulent jets (Fagherazzi et al., 2015). Typical features are subaqueous levees that extend basinward, and a prograding/aggrading mouth bar (Edmonds and Slingerland, 2007). However, all three previously mentioned studies base their findings on Delft3D models (Yuill et al., 2016; Fagherazzi et al., 2015; Edmonds and Slingerland, 2007). Therefore, output, including from this study, should be interpreted carefully. The convergence to turbulent-jet type systems could be a result of Delft3D not being able to fully capture the physics of turbulent flow.

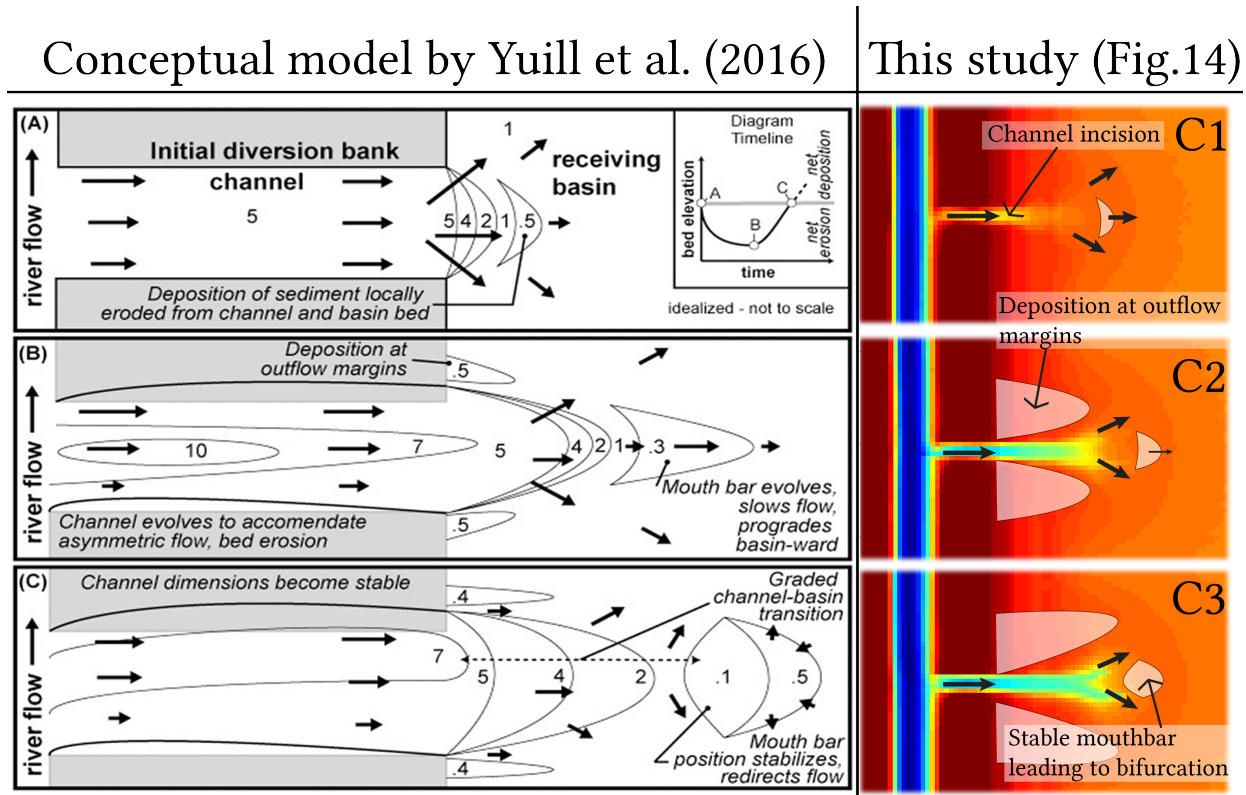


Figure 36: Similarity between Yuill et al. (2016) conceptual model and the model output from this study. The left part shows a conceptual illustration of three stages in the early life of a crevasse splay. Numbers are an indication for the relative depth and arrows indicate the depth-averaged flow magnitude and direction (Yuill et al., 2016). The right side shows the first three cycles from model MR-2. Please note the similar evolution of the crevasse-channel levees (deposition at outflow margins) and the mouth bar.

During the first flooding cycles water flows out of the river towards the floodplain. This is changed when the levee is incised deep enough for a reflux to occur during waning river discharge (fig. 37). During this last transport stage part of the sediment which was deposited onto the floodplain is transported back into the river channel. This decreases the netto sedimentation rate on the floodplain. The negative trend in sedimentation rate is amplified by the progradation of the crevasse-splay toe. Progradation of the system ( $\Delta L$  increases) has as a consequence that the hydrodynamic gradient, and hence, the transport capacity are lowered. The prospect is that this negative trend for the sedimentation rate will lead to the stabilization of the crevasse splay. However, whether or not the crevasse splay would fully heal itself is still uncertain.

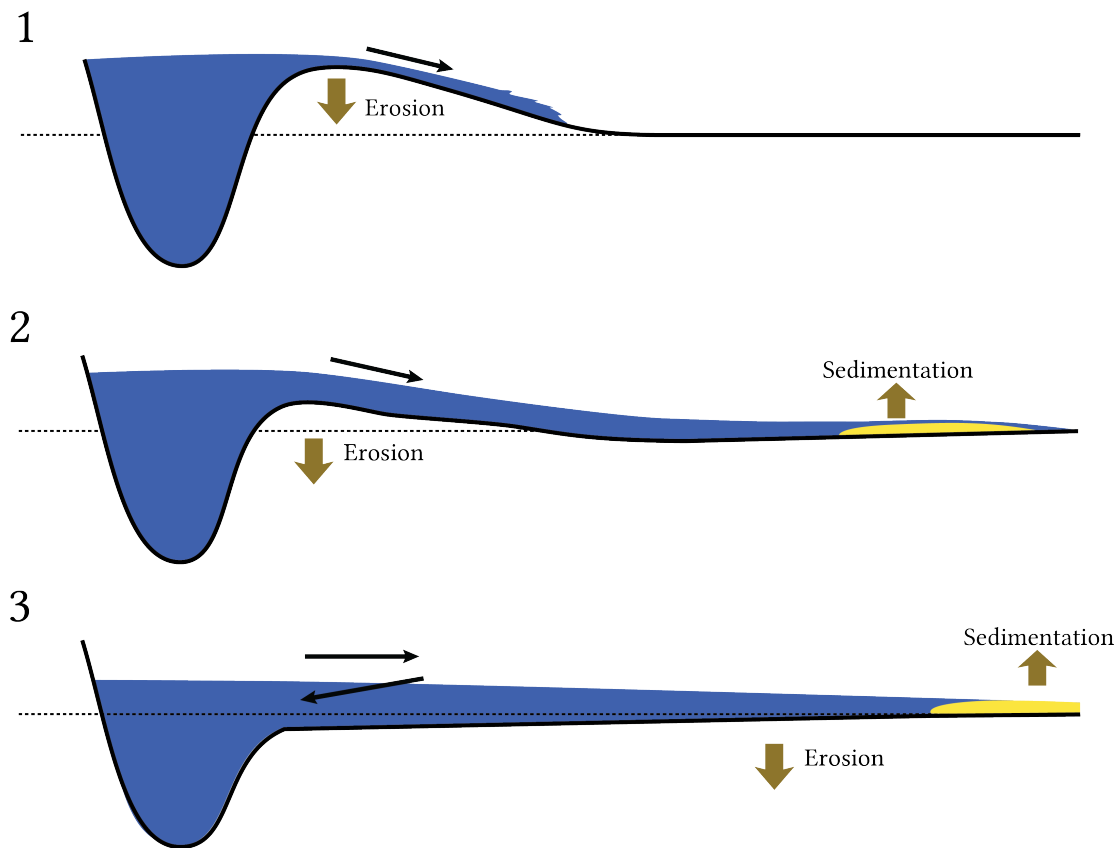


Figure 37: First three transport stages of a crevasse splay. It shows a conceptual cross section along the main crevasse-channel axis. 1) The initiation of a crevasse splay. The levee is breached and the breach point gets quickly eroded. 2) More water enters the floodplain. Crevasse channels are formed due to erosion and sediment is deposited lateral to and in the distal parts of the channels. 3) The base of the levee breach is eroded to an extent that water can flow back in the river during waning river flow. The crevasse-channel system is extended due to different erosional processes, including back-stepping erosion.

## 4.2 Crevasse-splay morphology

The observed dynamic behaviour has direct implications on the morphology. Interpreting the MR models, with the dynamic processes in mind, resulted in an architecture proposition that consists of three main elements:

1. Crevasse channel
2. Crevasse-channel-overbank deposits
3. Mouth bar

#### 4.2.1 Crevasse channel

Crevasse channels are the result of a confined flux bursting through the levee breach. Incision in the substrate indicates that water flowing out of the river has the capacity to transport additional sediment. The added transport capacity is a function of water velocity. This makes the magnitude of the erosion a direct function of flow energy, and hence, a function of the driving hydrodynamic gradient and the degree of confinement.

**Reflux** The model results show a crevasse-channel system with a decreasing incision depth from its apex to its fringes. The result is a negative bed-level gradient, which leads to a hysteresis for flux in and out of the river channel. Bagnold (1966) showed that bed-load transport is partly gravity driven and hence related to the bed gradient. This correlation is the driving force of the higher bed-load rates during the reflux stage. Note that a fixed bed-load to suspended-load ratio is used. The model corrects for the bed-slope effect and upstream bed composition and sediment availability. The resulting bed-load flux quantities are, hence, highly uncertain.

The result of a large sediment-load during reflux is the deposition of sediment at the lee zones situated lateral to the levee breach. The downstream reflux bars have been observed in the Río Colorado fluvial systems (Donselaar et al., 2013). These bars have also been observed in the 2014 field campaign. They form a crevasse-mouth complex with a "mouth bar" connecting the up-and downstream reflux bars (fig. 38). The models show that the sediment forming these bars is transported from the floodplain, through the crevasse channel, and deposited in the river channel. Given that the sediment bodies are preserved, it could be argued that the crevasse-mouth complex can connect the crevasse-channel and river-channel lag.

The morphology of this complex is dependent on the hydrodynamic response of the system. The behaviour of bifurcations is mainly controlled by the bed-gradient of the channels, the angle between them, and the curvature of the upstream channels (Kleinhans et al., 2012). In this study an orthogonal junction, where the river has the bed-gradient advantage, is simulated. This limits the field of research to these type of junctions. Extrapolating the models output to non-representative river-crevasse-channel junctions is inadvisable.

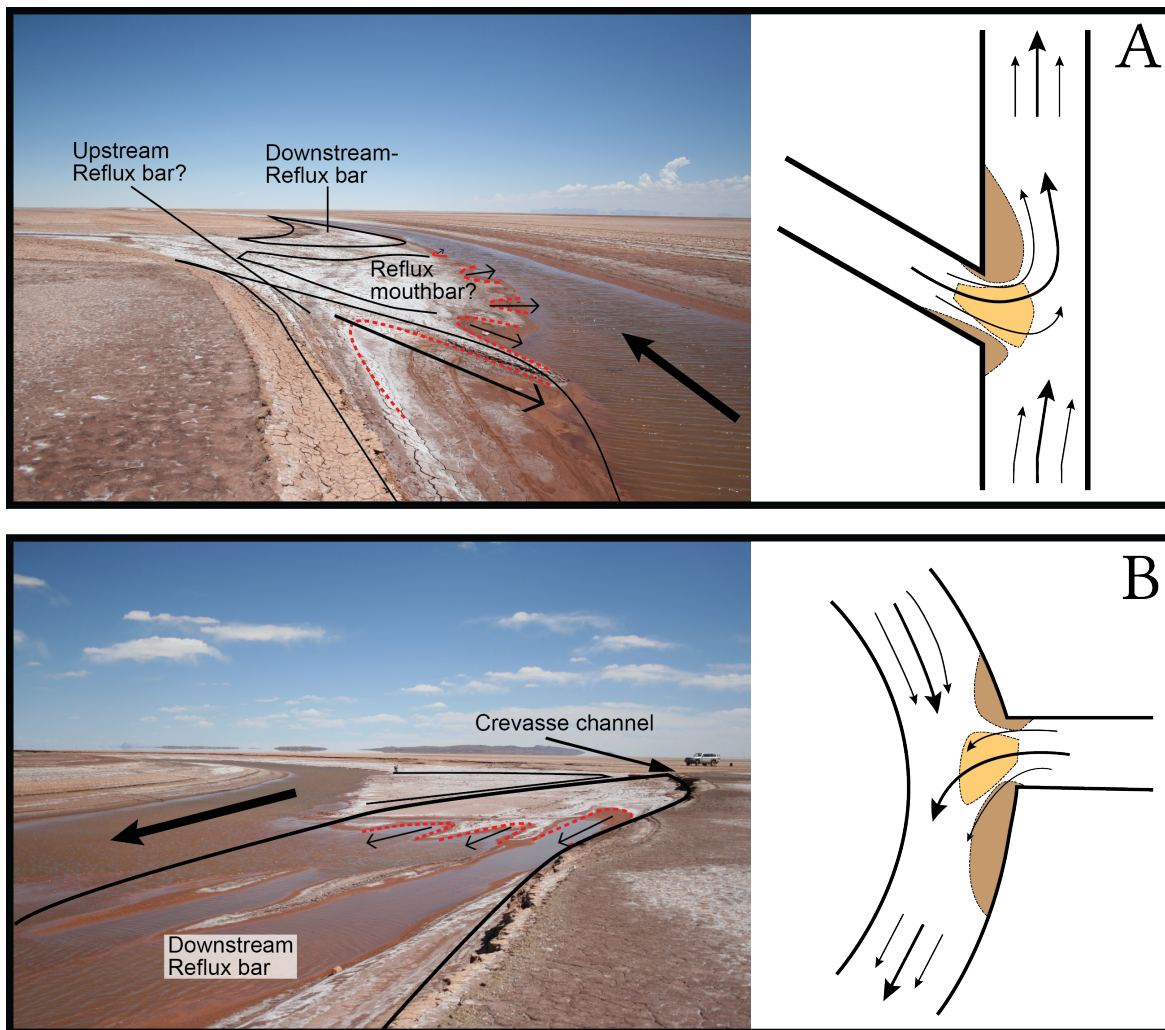


Figure 38: Left: Two photographs of different crevasse-mouth complexes as observed in the 2014 field-campaign. Right: A corresponding conceptual drawing with an interpretation of the flow during the reflux stage. A) shows a crevasse-channel oriented  $\pm 70^\circ$  from the river channel. B) shows a crevasse-channel oriented  $\pm 90^\circ$  from a curved river channel. Note the difference in morphology.

**Natural dimensions** Simulations showed incisive channels dimensions up to 90 cm deep and 15m wide. This gives a width-to-thickness ratio of 17 and a cross-sectional area of 20 m<sup>2</sup>. Field observations from a variety of fluvial deposits, measured a width-to-thickness ratio in the range 5-60 and absolute thicknesses less than 4 meters (Mjos et al., 1993). They show increasing incision depth over time with the river channel depth as maximum (Donselaar et al., 2013). These observations comply with the results of the process-based model.

**Channel Fill** Data from literature is mainly derived from fossil crevasse-channel bodies. This means that they have been filled with sediment. The process-based models don't show any sedimentation in the channel. It implies that the backfilling in crevasse channels happens in a later stage of a crevasse-channels life. This last backfilling stage remains still a poorly understood process. Analogue to river-channel fill, crevasse-channel sands could be deposited as channel-lag sands. Aggradation is conditional for this type of deposition (van Toorenburg et al., 2016). A second option is discussed by Slingerland and Smith (2004). They described a in-crevasse-channel deposition of side-channel bars. This deposition occurs when the discharge through the

levee breach is too small for the capacity of the crevasse channel. This low discharge could be i.a. the result of an upstream crevasse splay draining water from the river.

#### 4.2.2 Crevasse-channel-overbank deposits

The MR models show that the capacity of the crevasse channel is not sufficient to handle the amount of water entering the floodplain. The excessive water finds its way onto the crevasse channels overbank areas. The sediment is mainly transported as suspended load. The fraction of bed-load sediment decreases when it is transported up a slope as the model accounts for the bed-slope effect (van Rijn, 1993). The result is a diffusive sedimentation that is governed by relations based on the sediment properties (Partheniades, 1965; van Rijn, 1993). Overbank behaviour of large scale river systems could serve as an analogue.

**Natural crevasse-splay dimensions** Simulations showed a total areal dimensions of 200-300m in width and 100-150m in length. The average thickness amounts to 10-20cm. This gives a width-to-thickness ratio of 2000 and approximated area of 1,400,000 m<sup>2</sup>. Field observations from a variety of fluvial deposits, observed a width-to-thickness ratio in the range 150-1000 and absolute thicknesses of 0.3-4.5 m (Mjos et al., 1993) and 0.05-0.6m (van Toorenburg et al., 2016). 'New' crevasse splays from the Río Colorado fluvial system show an area of 1,300,000-5,000,000 m<sup>2</sup> (Li and Bristow, 2015). The model output values fall within the range of dimensions presented by literature. The exception is the areal extent where it shows a lower value then the observed values.

#### 4.2.3 Mouth bar

The coarser material of the system is transported through the channel, and settles when the flow energy becomes low enough. The behaviour of this mouth bar is, hence, dependent on the availability and size of the sediment, and the flow energy. Their interrelationship changes over time as the crevasse splay evolves. The dynamic behaviour of a crevasse splay can be subdivided in three categories (fig. 39).

- Progradation
- Bifurcation
- Stabilization

**Progradation** A mouth bar is initially deposited just beyond the most distal point of the crevasse-channels levees. During the early stage, the jet entering the floodplain has a high transport capacity. The transport capacity is further increased as the the streamlines are forced over the higher situated mouth bar (Edmonds and Slingerland, 2007). For a flow potential larger then a critical value, the the upstream part of the mouth bar is eroded. Consequently, on the lee side of the mouth bar, sediment is deposited, which results in the progradation of the mouth bar (Edmonds and Slingerland, 2007). Cross sections from MR models show coarser grained wings attached to the crevasse channel. Based on their location, shape and composition these wings are interpreted to be the remains of prograded mouth bar.

**Bifurcation** When the mouth bar has prograded to a critical distance from the apex, the local flow potential is not sufficient to erode the downstream part of the the mouth bar. Given that the mouth bar has aggraded to a critical height, water will start to flow around it (Fagherazzi et al., 2015). This is the case for both the flux towards and back to the river channel. The result is an bifurcation. Model MR-2 showed that this bifurcation

is not stable, leading to a main branch that incises further into the floodplain and a waning branch ending in a mouth bar. This instability is observed and modelled in previous work (Slingerland and Smith, 1998; Kleinhans et al., 2012).

**Stabilization** A mouth bar stabilizes when it stops prograding, while it has not aggraded to a critical height. The result is an accumulation of sediment between the tips of the crevasse-channel levee. Crescent shaped river mouth bars observed in the Apalachicola Delta could serve as an analogue for these kind of deposits (Fagherazzi et al., 2015).

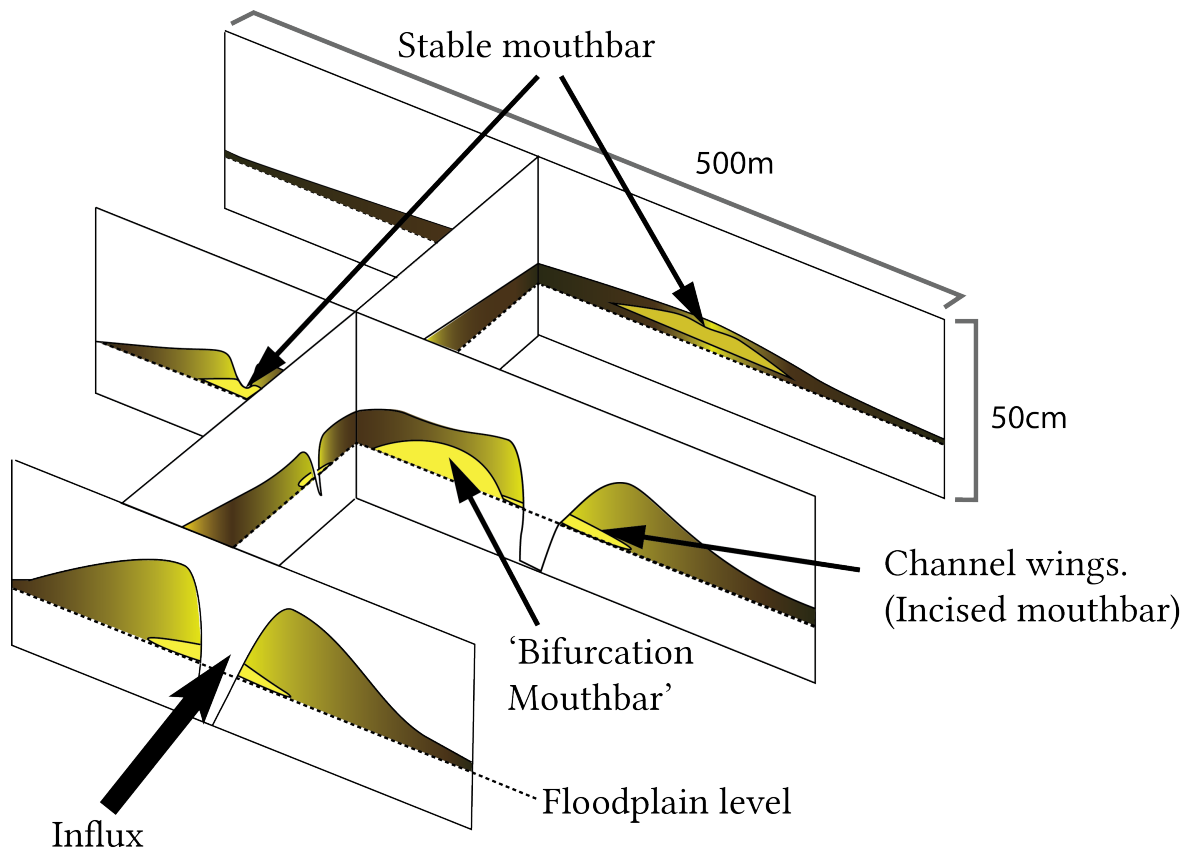


Figure 39: Conceptual architecture of crevasse channels, mouth bars and overbank deposits. The drawing is based on an assemble of cross sections from model MR-2.

#### 4.2.4 Crevasse splay architecture

A crevasse splay can be seen as a lower-order scale fluvial fan nested in a larger scale fluvial system. The modelled crevasse splay shows elements which make up the depositional model proposed by Fielding (1984). This model predicts a crevasse sub-delta with crevasse channels that feed lobe shaped extensions (fig. 40). This make-up of the different elements is in line with the architecture observed in the process-based model.

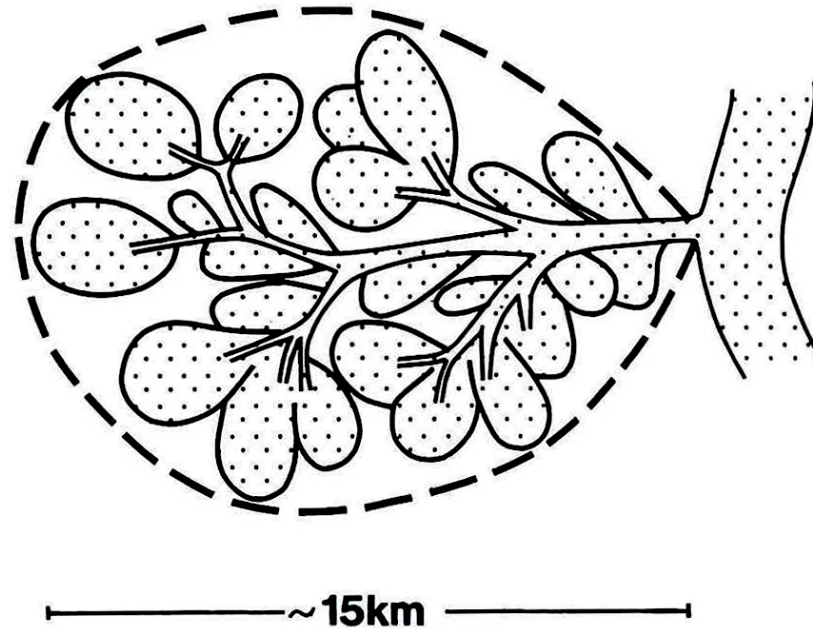


Figure 40: Depositional model after (Fielding, 1984). From: Mjos et al. (1993).

A generic depositional model may be represented as a network of active and (partially) abandoned crevasse channels with their corresponding mouth bar and overbank deposits. The result is a plano-convex sediment accumulation consisting of concatenated crevasse channels and mouth bars, which are encapsulated in overbank deposits. Their exact configuration is controlled by the behaviour of the hydrodynamic system, which on its turn is controlled by the sediment properties and pre-existing morphological features. These unique boundary conditions cannot be modelled. The (stochastic) placement of the architectural elements should be based on larger scale field observations.

### 4.3 Sedimentary trends & their relation to crevasse channels

The model shows sedimentary trends that are correlated with their relative location to a crevasse and/or river channel. This is in line with the hypothesis that sediment distribution is correlated with flow energy. However, a quantitative comparison between the average mean grain sizes shows significant difference between the model and reality.

The 2014 field campaign data from CS-1 shows an 50-100%<sup>4</sup> decrease in average mean grain size for a 10 meter increase in distance-to the crevasse channel. The model shows a more gradual decrease in mean grain size where a 100% decrease is reached at at more then 80 meters from the crevasse channel (fig. 41). This implies that applying this model for quantitative grain-size research is not valid. However, the model confirms observed trends like a decreasing grain-size for a longer distance-from the channel. A logical follow-up question would be: is it possible to improve the calibration of these models to enhance their qualitative accuracy?

<sup>4</sup>A 100% decrease is the equivalent of a factor 2. For example from 80 to 40  $\mu\text{m}$ .

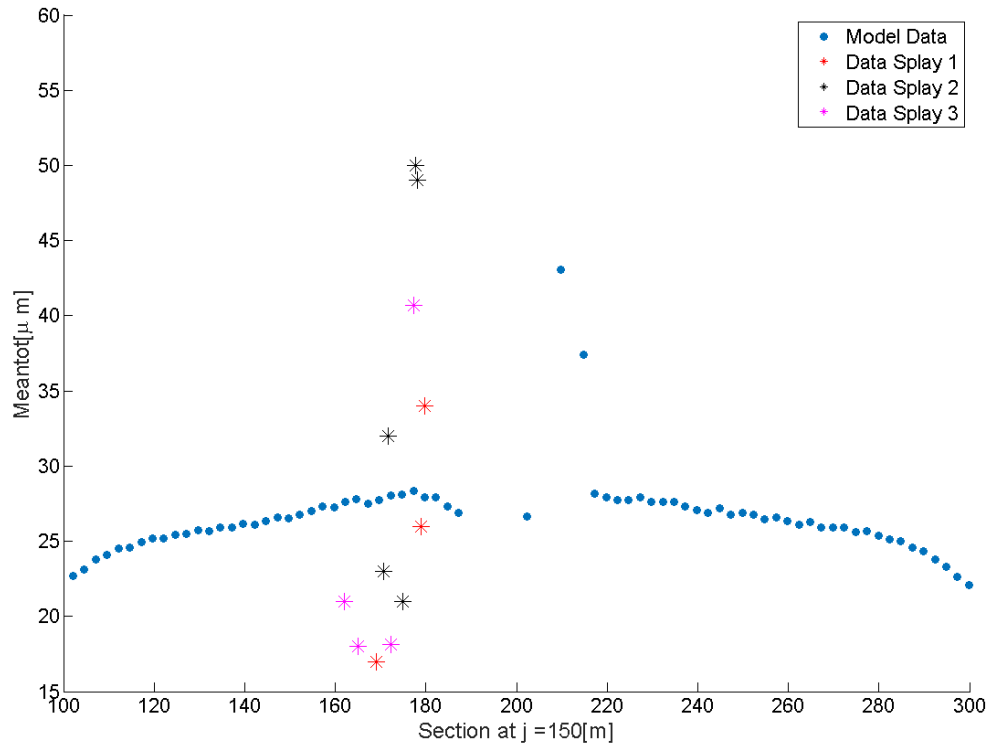


Figure 41: Average mean data vs distance-to channel from the 2014 field campaign. The edge of the simulated crevasse channel ( $x=180\text{m}$ ) was used calibration value for distance-from channel = 0. The data filtered for distance-in channel values of 0-120m and depth values of 10cm. The data is plotted together with average mean grain sizes from a cross section situated 60 meters longitudinally from the levee breach.

There are multiple possibilities as to why the model does not reproduce one-on-one representative grain-size relations. They fall in two categories:

1. Wrong input parameters
2. Model-errors

**Wrong input parameters** The sediment properties are derived from generic correlations. They could easily be under/over estimated. The steeper decline in grain-size as seen in the data could be explained by an underestimation of the smaller fraction's settling velocity. A reason for this under estimation could be that small individual grains can be transported as aggregates. These aggregates will behave as larger grain particles and hence, will settle at higher speeds (Hawley, 1982).

**Model-errors** A model is a simplified representation of nature. This means that errors due to discretisation and simplification of natural processes are bound to occur. Delft3D governing equations concerning sediment transport are mostly empirically derived and the question remains if the model captures all physical controls on deposition.

#### 4.4 Compensational stacking

The amalgamation of crevasse splays can positively contribute to the total of connected pore volume. Both vertical (van Toorenburg et al., 2016) and lateral amalgamation (Donselaar et al., 2013; Li et al., 2014) have been observed in fossil and modern-day deposits, respectively. The process-based model results show that a crevasse splay can nest itself between two pre-existing crevasse splays. The resulting cross sections show a good resemblance with the compensational stacking concept proposed by Li et al. (2014) (fig. 42).

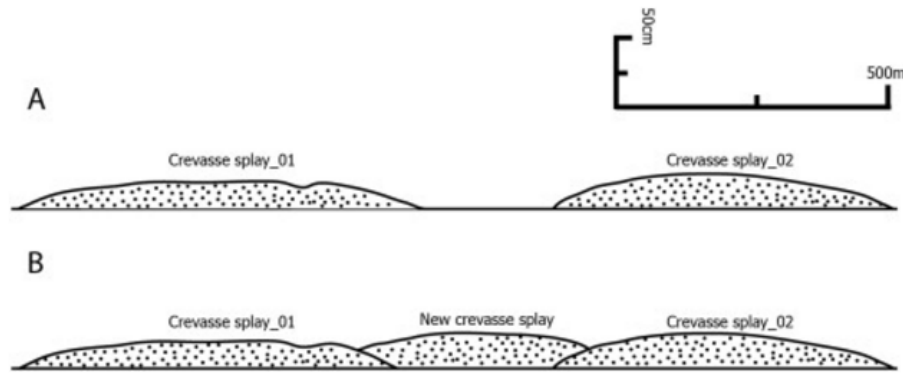


Figure 42: Concept of compensational stacking of single crevasse splays. A shows two pre-existing crevasse splays. In B a younger crevasse-splay has nested between them. From Li et al. (2014).

The main concern for compensational stacking is the connectivity. Clay drapes deposited during the inundation phase can act as a permeability baffle. The models show that lateral connectivity is a function of the measure of confinement. The closer the pre-existing crevasse splays are together, the higher the flow energy, and thus, the erosion potential. However, simulations did not cover the effect of the clay properties. The possibility exists that a very cohesive clay can prevent erosion. This can lead to the absence of an erosional contact.

#### 4.5 Petrophysical properties & Statistical error

Deriving in-situ reservoir properties from grain-size data is based on empirical correlations. In this study a grain-size-distribution based correlation is used to estimate the porosity ( $\phi$ ) and permeability ( $k$ ) during deposition. In-situ  $\phi$  &  $k$  values were estimated by taking into account the mechanical compaction. In addition, it is commonly assumed that other diagenetic processes can significantly alter the rock properties during burial (Morad et al., 2010). The sheer number of unknown parameters needed to translate grain-size data into in-situ reservoir properties makes them highly uncertain. A calibration of the model output with reliable core-plug measurements is therefore still essential.

Comparison with sub-surface core measurements shows that the in-situ permeability and porosity values from the model ( $k = 0.01 - 0.15\text{mD}$ ,  $\phi = 0.06 - 0.12$ ) are in the same order of magnitude as the silty crevasse splays (table 5). This implies that the properties derived from this study's discrete model data may be used as a proxy for crevasse splays that are penetrated by the specific wells. However, if the rock is chemically and/or mechanically altered, the measured properties can significantly deviate from the predicted values. How to, subsequently, correctly calibrate the data is still unknown and could be a topic for further research.

| Well       | Depth[m] | Porosity[%] | Horz. Perm [mD] | Grain size      |
|------------|----------|-------------|-----------------|-----------------|
| OBLZ-01    | 2215.33  | 14          | 5               | very fine sand  |
| OBLZ-01    | 2215.33  | 14          | 6               | very fine sand  |
| GAG-03     | 3611     | 3           | 0.01            | Clay-Silt       |
| GAG-03     | 3612     | 1           | 0.01            | Very fine sand  |
| GAG-03     | 3612.25  | 2           | 0.02            | Very fine sand  |
| SPKO-10-S1 | 2652.85  | 8           | 0.15            | silt            |
| SPKO-10-S2 | 2653.15  | 17          | 14              | Very fine sand  |
| NM0026     | 2671.7   | 3           | 0.02            | Silt            |
| NM0026     | 2672     | 10          | 0.5             | very fine lower |
| NM0026     | 2672.3   | 9           | 0.4             | Silt            |

Table 5: Porosity and permeability core measurements from intervals interpreted as crevasse splay. All wells where drilled from the dutch sector. From: ongoing research performed by H.T.W. Boerboom. The raw data was derived from <http://www.nlog.nl/>.

It is key to minimize the statistical error to optimize the reliability of porosity and permeability estimations. For example, the equation used to determine permeability is quadratically related to the mean grain size. The observed minimum statistical error of 20% will result in a 40% deviation in the permeability values. Results from the statistical sensitivity analysis show that choosing the amount and size of discrete grain size classes is essential. In this study, the analysis was performed after the bins where chosen. In hindsight, a different sediment-set would have been more optimal. When modelling a system with bimodal Weibull grain-size distributions, a minimum of six bins is advised. A bimodal Weibull distribution has five degrees of freedom, meaning that it contains five independent variables. To mathematically solve for such a system, a minimum of six data points are needed. More generally, when modelling  $n$ -modal-distributed sediments, a minimum of  $n + 1$  grain-size classes are required.

A second type of error was related to the wrong bin value selection. For this thesis the exact determination of the grain-size per bin was determined based on a visual interpretation of grain-size distributions. The lowest class ( $7\mu\text{m}$ ) was too high to offer a useful anchorage for fitting the lower distribution. The unwanted result was that the small fraction was commonly overestimated. For future research, this grain-size picking process should be improved. For example by creating an algorithm that minimizes the error by selecting an optimal combination of grain-size classes.

## 5 Conclusions

It is possible to use a process-based model to study a crevasse splay governing processes and sedimentary architecture. Process-based simulations demonstrate the effect of different conditions through their direct influence on physical processes. Crevasse-splay formation only occurs for water levels that are higher than the base of the levee breach and lower than the top of the levee. The resulting crevasse-splay morphology is dependent on the relation between the driving hydrodynamic gradient and the counteracting frictional forces. Both outflow from the river onto the floodplain and reflux of water back into the river leads to an erosional channel network. Channels, together with their related overbank and mouth-bar deposits, form the architectural elements that make up crevasse splay. The proposed architecture shows similarities with previously-presented depositional models. Dimensions of the simulated crevasse-splay complex and its crevasse-splay channels fall within the range of spatial values observed in present-day and fossil fluvial systems.

Sedimentary trends are closely correlated with the different morphodynamic elements. The hypothesis that grain size is related to the flow energy is confirmed by the models output. Sediments deposited close to the channel show the most favourable reservoir properties. This research shows that these higher-permeability zones can be connected when individual crevasse-splay amalgamate laterally. The quality of connectivity is a.o. a function of distance between the pre-existing splay.

The petrophysical parameters were derived from continuous grain size distributions parameters. This study demonstrates a statistical approach to extract these from discrete grain-size data. A sensitivity study shows that using the right size and amount of grain-size classes is crucial to minimize errors. This could be investigated in further research.

The exact architecture of a larger scale crevasse-splay, as well as the sub-grid subtleties are not studied. A quantitative comparison was made between field and simulated data. It shows that the model overestimates the grain size as sediment is transported away from a channel. The conclusion is that this model is not valid for quantitative purposes.

The process-based model with its current abilities and limitations can be used as a tool for heuristic research. It allows the study of the different governing processes. These ideas should be taken back into the field to test, validate, and further study the exact morphodynamics of the system. Resulting concepts can be used to accurately predict the crevasse-splay architecture and corresponding sedimentary trends. Subsequently these can be used as an input in reservoir models to improve their reliability.

## 6 Acknowledgements

This study received financial support from ENGIE E&P NL B.V., Energiebeheer Nederland B.V. (EBN), the Molengraaff Fund (SMGF), and the Delft University Fund (UfD). The simulations were carried out on the Dutch national e-infrastructure with the support of SURF Foundation (NWO project MP-293-14). I would like to thank Rick Donselaar and Joep Storms for their guidance and gentle push to submit my work for two EAGE conferences. My special thanks goes to Koen van Tooreneburg and Helena van der Vegt who spent a lot of their time helping me out. Last but not least, I want to thank my partner in crime Herman Boerboom for sitting 9 months beside me and the many discussions we could have on crevasse-splays.

## References

- Bagnold, R. A. (1966). *An approach to the sediment transport problem from general physics*. Geological Survey professional paper 422-I. U.S. Govt. Print. Off.
- Bahr, B. D., Hutton, E. W. H., and Syvitski, J. P. M. (2001). Exponential approximations to compacted sediment porosity profiles. *Computer & Geosciences*, 27:691–700.
- Bridge, J. S. (2006). In Posamentier, H.W. and Walker, R.G. (Eds.) *Facies Models Revisited*, volume 84 of *Special Publications*, chapter Fluvial Facies Models: Recent Developments, pages 85–170. SEPM.
- Bristow, S. C., Skelly, L. R., and Ethridge, G. F. (1999). Crevasse splays from the rapidly aggrading, sand-bed, braided Niobrara River, Nebraska: effect of base-level rise. *Sedimentology*, 46:1029–1048.
- Bürkholz, A. and Polke, R. (1984). Laser Diffraction Spectrometers/Experience in Particle Size Analysis. *Particle & Particle Systems Characterization*, 1:153–160.
- Cheng, N. S. (1997). Simplified Settling Velocity Formula for Sediment Particle. *Journal of Hydraulic Engineering*, 123:149–152.
- Dalman, F. R. A. and Weltje, G. J. (2008). Sub-grid parameterisation of fluvio-deltaic processes and architecture in a basin-scale stratigraphic model. *Computers & Geosciences*, 34:1370–1380.
- Dastgheib, A., Roelvink, A. J., and Wang, B. Z. (2008). Long-term process-based morphological modeling of the Marsdiep Tidal Basin. *Marine Geology*, 256:90–100.
- Donselaar, M. E., Cuevas Gozalo, M. C., and Moyano, S. (2013). Avulsion processes at the terminus of low-gradient semi-arid fluvial systems: Lessons from the Río Colorado, Altiplano endorheic basin, Bolivia. *Sedimentary Geology*, 283:1–14.
- Donselaar, M. E., Overeem, I., Reichwein, J. H., and Visser, C. A. (2011). Mapping of fluvial fairways in the Ten Boer Member, southern Permian Basin. *The Permian Rotliegend in the Netherlands: SEPM Special Publication*, 98:105–118.
- Edmonds, D. A. and Slingerland, R. L. (2007). Mechanics of river mouth bar formation: Implications for the morphodynamics of delta distributary networks. *Journal of Geophysical Research*, 112:F02034.
- Engelund, F. and Hansen, E. (1976). *a monograph on sediment transport in alluvial streams*. Technical University of Denmark.
- Fagherazzi, S., Edmonds, D. A., Nardin, W., Leonardi, N., Canestrelli, A., Falcini, F., Jerolmack, D. J., Mariotti, G., Rowland, J. C., and Slingerland, R. L. (2015). Dynamics of river mouth deposits. *Reviews of Geophysics*, 53:642–67.
- Fielding, C. R. (1984). A coal depositional model for the Durham Coal measures of NE England. *J. Geol. Soc. Lond.*, 42:41–48.
- Guoren, D. (2000). Incipient motion of sediment under currents. *China Ocean Engineering*, 14(4):7–9.
- Hajek, A. E. and Edmonds, A. D. (2014). Is river avulsion style controlled by floodplain morphodynamics? *Geology*, 42:199–202.
- Hajek, E. A. and Wolinsky, M. A. (2012). Simplified process modeling of river avulsion and alluvial architecture: Connecting models and field data. *Sedimentary Geology*, 257-260:1–30.
- Hawley, N. (1982). Settling velocity distribution of natural aggregates. *Journal of geophysical research*, 87:9489–9498.

- Jiménez, A. J. and Madsen, S. O. (2003). A simple formula to estimate settling velocity of natural sediments. *Journal of waterway, port, coastal, and ocean engineering*, 129:70–78.
- Kleinhans, M., Ferguson, G. I., Lane, S. N., and Hardy, J. (2012). Splitting rivers at their seams: bifurcations and avulsion. *Earth Surface Processes and Landforms*, 38:47–61.
- Leendertse, J. J. (1987). A three-dimensional alternating direction implicit model with iterative fourth order dissipative non-linear advection terms. *Rep. WD-3333-NETH, Rijkswaterstaat, The Netherlands*.
- Lesser, R. G., Roelvink, A. J., van Kester, M. J. A. T., and Stelling, S. G. (2004). Development and validation of a three-dimensional morphological model. *Coastal engineering*, 51:883–915.
- Li, J. and Bristow, C. S. (2015). Crevasse splay morphodynamics in a dryland river terminus: Río Colorado in Salar de Uyuni Bolivia. *Quaternary International*, 377:71–82.
- Li, J., Donselaar, M. E., Hosseini Aria, S. E., Koenders, R., and Oyen, A. M. (2014). Landsat imagery-based visualization of the geomorphological development at the terminus of a dryland river system. *Quaternary International*, 352:100–110.
- Mjos, R., Walderhaug, O., and Prestholm, E. (1993). Crevasse splay sandstone geometries in the Middle Jurassic Ravenscar Group of Yorkshire, UK. *Alluvial Sedimentation, International Association of Sedimentologists, Special Publication*, 17:167–184.
- Morad, S., Al-Ramadan, K., Ketzer, J. M., and De Ros, L. (2010). The impact of diagenesis on the heterogeneity of sandstone reservoirs: A review of the role of depositional facies and sequence stratigraphy. *AAPG bulletin*, 94(8):1267–1309.
- Nichols, G. J. and Fisher, J. A. (2007). Processes, facies and architecture of fluvial distributary system deposits. *Sedimentary Geology*, 195:75–90.
- O'Brien, E. P. and Wells, T. A. (1986). A small, alluvial crevasse splay. *Journal of Sedimentary Research*, 56:876–879.
- Ouchiyaama, N. and Tanaka, T. (1989). Predicting the densest packings of ternary and quaternary mixtures of solid particles. *Industrial & Engineering Chemistry Research*, 28:1530–1536.
- Panda, N. M. and Lake, W. L. (1994). Estimation of single-phase permeability from parameters of particle-size distribution. *AAPG Bulletin*, 78:1028–1039.
- Partheniades, E. (1965). Erosion and Deposition of Cohesive Soils. *Journal of the Hydraulics Division*, 34:105–139.
- Rhee, C. W. and Chough, S. K. (1993). The Cretaceous Pyonghae Basin, southeast Korea: sequential development of crevasse splay and avulsion in a terminal alluvial fan. *Sedimentary Geology*, 83:37–52.
- Roberts, J., Jepsen, R., Gotthard, D., and Lick, W. (1998). Effects of particle size and bulk density on erosion of quartz particles. *Journal of Hydraulic Engineering*, 124:1261–1267.
- Slingerland, R. and Smith, N. D. (1998). Necessary conditions for a meandering-river avulsion. *Geology*, 26:435–438.
- Slingerland, R. and Smith, N. D. (2004). River avulsions and their deposits. *Annu. Rev. Earth Planet. Sci.*, 32:257–285.
- Stelling, S. G., Wiersma, K. A., and Willemse, M. J. B. T. (1986). Practical aspects of accurate tidal computations. *Journal of Hydraulic Engineering*, 112:802–816.

- Sun, D., Bloemendal, J., Rea, D. K., Vandenberghe, J., Jiang, F., An, Z., and Su, R. (2002). Grain-size distribution function of polymodal sediments in hydraulic and aeolian environments, and numerical partitioning of the sedimentary components. *Sedimentary Geology*, 152:263–277.
- Tooth, S. (2005). Splay Formation Along the Lower Reaches of Ephemeral Rivers on the Northern Plains of Arid Central Australia. *Journal of Sedimentary Research*, 75(4):636–649.
- Torres Carranza, Y. A. (2013). Static Reservoir Model of Crevasse Splays in the Colorado River System, Salar of Uyuni, Bolivia. Master's thesis, Delft University of Technology.
- van Rijn, L. C. (1993). *Principles of sediment transport Part I*, . Principle of Sediment Transport in Rivers, Estuaries and Coastal Seas. Aqua publications Amsterdam.
- van Rijn, L. C. (2006). *Principle of Sediment Transport, Part II*. Principle of Sediment Transport in Rivers, Estuaries and Coastal Seas. Aqua publications Amsterdam.
- van Tooreneburg, K. A., Donselaar, M. E., Noordijk, N. A., and Weltje, G. J. (2016). On the origin of crevasse-splay amalgamation in the Huesca fluvial fan (Ebro Basin, Spain): Implications for connectivity in low net-to-gross fluvial deposits. *Sedimentary Geology*, 343:156–164.
- Weber, K. J. and van Geuns, L. C. (1990). Framework for Constructing Clastic Reservoir Simulation Models. *Journal of Petroleum Technology*, 42:1248–1297.
- Weltje, G. J. and Prins, M. A. (2007). Genetically meaningful decomposition of grain-size distributions. *Sedimentary Geology*, 202:409–424.
- Yu, B. A. and Standish, N. (1991). Estimation of the porosity of particle mixtures by a linear-mixture packing model. *Industrial & Engineering Chemistry Research*, 30:1372–1385.
- Yu, B. A. and Standish, N. (1993). A study of the packing of particles with a mixture size distribution. *Powder Technology*, 76:113–124.
- Yuill, T. B., Khadka, A. K., Pereira, J., Allison, M. A., and Meselhe, E. A. (2016). Morphodynamics of the erosional phase of crevasse-splay evolution and implications for river sediment diversion function. *Geomorphology*, 259:12–29.
- Zanke, E. U. C. (2003). On the influence of turbulence on the initiation of sediment motion. *International Journal of Sediment Research*, 18:17–31.

## A The Río Colorado fluvial fan

The Río Colorado fluvial fan is situated in the Altiplano Basin, Bolivia. The system currently experiences a base-level lowstand, resulting in a prograding river system on a low-gradient coastal plain (Donselaar et al., 2013). Ephemeral peak-discharge events, triggered by seasonal rains, result in massive flooding and the formation of over- and through- bank deposition.

Crevasse splays start of as small lobes with an acreage of  $42 \times 10^3 \text{m}^2$ , and can grow within 15 years to a complex distributary channel network covering  $2,5 \times 10^6 \text{m}^2$  (Li et al., 2014). Compensational stacking of the different units is observed and provided that there's 'sand-on-sand contact' it offers huge volumetric potential in the form of thin extensive sheets.

## B SF models

| Model Name  | Run-time | $\Delta t$ (s) | Inflow           | Outflow            | Dry Points | Notes                          |
|-------------|----------|----------------|------------------|--------------------|------------|--------------------------------|
| Model SF-1  | 2h       | 0.01           | V/1.5/0.5/180/90 | WL/4.9/0.55/180/90 | Yes        | Levee breach +inundation       |
| Model SF-2  | 2h       | 0.01           | V/1.5/0.5/180/90 | WL/4.9/0.55/180/90 | No         | Crash. Water over levee at BC1 |
| Model SF-3  | 10h      | 0.01           | V/1.5/0.5/180/90 | WL/4.9/0.55/180/90 | No         | Crash. Water over levee at BC1 |
| Model SF-4  | 10h      | 0.01           | V/1.5/0.5/180/90 | WL/4.9/0.55/180/90 | Yes        | Levee breach +inundation       |
| Model SF-5  | 10h      | 0.01           | D/20/10/180/90   | WL/4.9/0.55/180/90 | Yes        | Levee breach +inundation       |
| Model SF-6  | 10h      | 0.01           | D/20/10/180/90   | WL/4.9/0.55/180/90 | No         | Crash. Water over levee at BC1 |
| Model SF-7  | 10h      | 0.01           | D/20/10/90/90    | WL/4.9/0.55/90/90  | No         | Levee breach (Unstable model)  |
| Model SF-8  | 10h      | 0.01           | D/15/5/180/90    | WL/4.9/0.55/180/90 | No         | No breach                      |
| Model SF-9  | 10h      | 0.01           | D/15/5/90/90     | WL/4.9/0.55/90/90  | No         | No breach                      |
| Model SF-10 | 10h      | 0.01           | D/20/10/90/90    | WL/4.9/0.60/90/90  | No         | Levee breach +inundation       |
| ModelSF-14  | 10h      | 0.01           | Time series t    | WL/4.9/0.60/90/90  | No         | Levee breach +inundation       |

Table 6: The first models from the SF series. The goal was to explore the effect of the boundary conditions. A cyclic inflow and outflow boundary conditions were used. The boundary conditions are noted as: Type of boundary condition/maximum value/minimum value/frequency/phase. With V(elocity), D(ischarge), W(ater)L(evel).

| Model Name   | $\alpha$ | Rk   | Suspuc | Notes                                      |
|--------------|----------|------|--------|--|
| Model SF-4   | 1        | 0.06 | 0.08   |  |
| Model SF-4-1 | 0.9      | 0.06 | 0.8    | Channels well visible                      |
| Model SF-4-2 | 0.7      | 0.06 | 0.8    | Less sediment on floodplain                |
| Model SF-4-3 | 1        | 0.03 | 0.8    | No significant difference with SF-4        |
| Model SF-4-4 | 1        | 0.12 | 0.8    | No significant difference with SF-4        |
| Model SF-4-5 | 1        | 0.06 | 0.7    | Sediment more concentrated around channels |
| Model SF-4-6 | 1        | 0.06 | 0.9    | More diffusive sediment on floodplain      |

Table 7: This series where used to explore the effect of the Engelund-Hansen transport formula.  $\alpha$  = correlation coefficient. Rk = roughness height for currents. Suspuc is the set fraction of suspended load.

| Model Name  | Correlation     | Coefficient | Notes                      |
|-------------|-----------------|-------------|----------------------------|
| ModelSF-6   | Chezy           | 70          |                            |
| ModelSF-6R1 | Chezy           | 55          | Crash                      |
| ModelSF-6R2 | Chezy           | 80          | Crash                      |
| ModelSF-6R3 | White-Colebrook | 0.15        | Crash                      |
| ModelSF-6R4 | White-Colebrook | 0.1         | Crash                      |
| ModelSF-6R5 | Manning         | 0.2         | Crash                      |
| ModelSF-6R6 | Manning         | 0.3         | Almost same result as SF-6 |

Table 8: This series where used to explore the effect of the bottom roughness coefficients

| Model Name   | Morfac | Note                                       |
|--------------|--------|--|
| ModelSF-4    | 60     | Shows instabilities at boundary conditions |
| ModelSF-4MF1 | 50     | Shows instabilities at boundary conditions |
| ModelSF-4MF2 | 30     | Shows instabilities at boundary conditions |
| ModelSF-4MF3 | 20     | Stable. Sediment pack on floodplain >10cm  |
| ModelSF-4MF4 | 1      | Stable. Sediment pack on floodplain <5 cm  |
| ModelSF-6    | 60     | Shows instabilities at boundary conditions |
| ModelSF-6MF1 | 30     | Shows instabilities at boundary conditions |

Table 9: This series where used to explore the effect of the morphological factor

| Model Name  | Scheme momentum | Scheme Transport | DaGC |
|-------------|-----------------|------------------|------|
| ModelSF-6   | Flood           | Cyclic           | Min  |
| ModelSF-6N1 | Flood           | van leer         | Min  |
| ModelSF-6N2 | Cyclic          | Cyclic           | Min  |
| ModelSF-6N3 | Flood           | Cyclic           | Max  |

Table 10: This series where used to explore the effect of the numerical transport schemes

| Modelname      | Inflow        | Outflow              | Bottom Roughness |
|----------------|---------------|----------------------|------------------|
| Model SF-11    | D/20/10/90/90 | WL/5.0/0.55/90/90    | M0.02            |
| Model SF-12    | D/25/10/90/90 | WL/5.1/0.55/90/90    | M0.02            |
| Model SF-121   | D/25/10/90/90 | WL/5.1/0.55/90/90    | M0.025           |
| Model SF-122   | D/25/10/90/90 | WL/5.1/0.55/90/90    | M0.03            |
| Model SF-13    | D/25/10/90/90 | WL QH/0-4.21/35-5.55 | M0.02            |
| Model SF-13M02 | D/25/10/90/90 | WL QH/0-4.21/35-5.55 | M0.01            |
| Model SF-13SL1 | D/25/10/90/90 | WL QH/0-4.21/35-5.55 | M0.02            |
| ModelSF13M02   | D/25/10/90/90 | WL QH/0-4.21/35-5.55 | M0.015           |

Table 11: This series where used to explore the combined effect of boundary conditions and bottom roughness.

## C MR models

| $7\mu m$          | low      | med      | high     |
|-------------------|----------|----------|----------|
| $\tau_{cr,b,ero}$ | 1.50E-02 | 3.00E-02 | 6.00E-02 |
| $\tau_{cr,b,sed}$ | 1.00E+03 | 1.00E+03 | 1.00E+03 |
| $V_{set}$         | 1.09E-04 | 2.17E-04 | 4.34E-04 |
| $C_{ero}$         | 1.00E-05 | 1.00E-04 | 1.00E-03 |
| $25\mu m$         | low      | med      | high     |
| $\tau_{cr,b,ero}$ | 2.75E-02 | 5.50E-02 | 1.10E-01 |
| $\tau_{cr,b,sed}$ | 1.00E+03 | 1.00E+03 | 1.00E+03 |
| $V_{set}$         | 6.80E-04 | 1.36E-03 | 2.72E-03 |
| $C_{ero}$         | 1.00E-05 | 1.00E-04 | 1.00E-03 |
| $45\mu m$         | low      | med      | high     |
| $\tau_{cr,b,ero}$ | 4.00E-02 | 8.00E-02 | 1.60E-01 |
| $\tau_{cr,b,sed}$ | 1.00E+03 | 1.00E+03 | 1.00E+03 |
| $V_{set}$         | 2.20E-03 | 4.40E-03 | 8.80E-03 |
| $C_{ero}$         | 1.00E-05 | 1.00E-04 | 1.00E-03 |

Table 12: Properties of the cohesive sediment fractions, used for the MR models.

| MR ModelNames  | TcrEro | SetV | EroPar | Note  |
|----------------|--------|------|--------|---|
| ModelMR-2SED1  | Med    | Med  | Med    | 1 Bifurcation, Deep channels                    |
| ModelMR-2SED2  | Min    | Med  | Med    | 1 Bifurcation,Very deep channels                |
| ModelMR-2SED3  | Max    | Med  | Med    | 1 Bifurcation, less deep channels               |
| ModelMR-2SED4  | Max    | Max  | Med    | 1 Bifurcation, less deep channels,higher levees |
| ModelMR-2SED5  | Min    | Min  | Med    | 1 Bifurcation, very deep channels,higher levees |
| ModelMR-2SED6  | Med    | Min  | Med    | 1 Bifurcation, less high crevasse levees        |
| ModelMR-2SED7  | Med    | Max  | Med    | 1 Bifurcation, high crevasse levees             |
| ModelMR-2SED8  | Med    | Med  | Min    | 1 Bifurcation, less deep channels               |
| ModelMR-2SED9  | Med    | Med  | Max    | 1 Bifurcation,Very deep channels                |
| ModelMR-2SED10 | Med    | Max  | Min    | 1 Bifurcation, less deep channels,higher levees |
| ModelMR-2SED11 | Max    | Max  | Min    | 1 Bifurcation, less deep channels,higher levees |

Table 13: MR models testing different sediment properties for the cohesive sediment fractions. For exact values see table 12

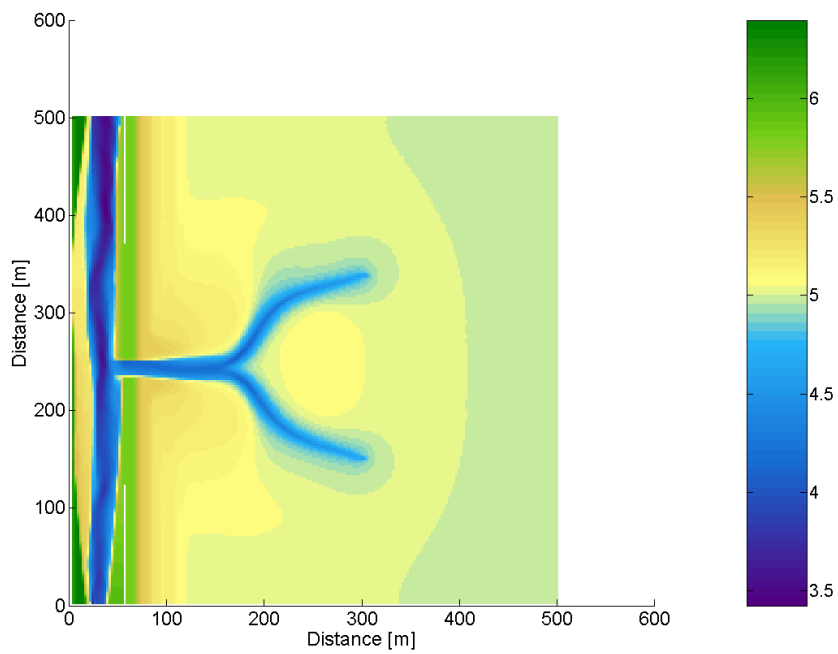


Figure 43: The output of model MR-2SED7. Note that the crevasse channel reaches a depth up to river-channel depth.

## D SB models

Grain-size classes with a diameter of 7, 20, 40, 65 where used form the SB models

| $7\mu m$          | low      | med      | high     |
|-------------------|----------|----------|----------|
| $\tau_{cr,b,ero}$ | 1.50E-02 | 3.00E-02 | 6.00E-02 |
| $\tau_{cr,b,sed}$ | 1.00E+03 | 1.00E+03 | 1.00E+03 |
| $V_{set}$         | 1.09E-04 | 2.17E-04 | 4.34E-04 |
| $C_{ero}$         | 1.00E-05 | 1.00E-04 | 1.00E-03 |
| $20\mu m$         | low      | med      | high     |
| $\tau_{cr,b,ero}$ | 5.50E-02 | 1.10E-01 | 2.20E-01 |
| $\tau_{cr,b,sed}$ | 1.00E+03 | 1.00E+03 | 1.00E+03 |
| $V_{set}$         | 4.35E-04 | 8.70E-04 | 1.74E-03 |
| $C_{ero}$         | 1.00E-06 | 1.00E-05 | 1.00E-04 |
| $40\mu m$         | low      | med      | high     |
| $\tau_{cr,b,ero}$ | 5.00E-02 | 1.00E-01 | 2.00E-01 |
| $\tau_{cr,b,sed}$ | 1.00E+03 | 1.00E+03 | 1.00E+03 |
| $V_{set}$         | 1.75E-03 | 3.50E-03 | 7.00E-03 |
| $C_{ero}$         | 1.00E-06 | 1.00E-05 | 1.00E-04 |

Table 14: Different properties of the cohesive sediment fractions, used for the SB models.

| SB-ModelNames | TcrEro | SetV | EroPar |
|---------------|--------|------|--------|
| ModelSBSED1   | Med    | Med  | Med    |
| ModelSBSED2   | Min    | Med  | Med    |
| ModelSBSED3   | Max    | Med  | Med    |
| ModelSBSED4   | Med    | Min  | Med    |
| ModelSBSED5   | Med    | Max  | Med    |
| ModelSBSED6   | Med    | Med  | Min    |
| ModelSBSED7   | Med    | Med  | Max    |
| ModelSBSED8   | Max    | Max  | Min    |
| ModelSBSED9   | Min    | Max  | Min    |
| ModelSBSED10  | Max    | Max  | Max    |
| ModelSBSED11  | Max    | Min  | Min    |
| ModelSBSED12  | MaxMax | Max  | Min    |

Table 15: SB-models testing different sediment properties for the cohesive sediment fractions. For exact values see table 14

## E Cross sections MR-3 with sediment fractions

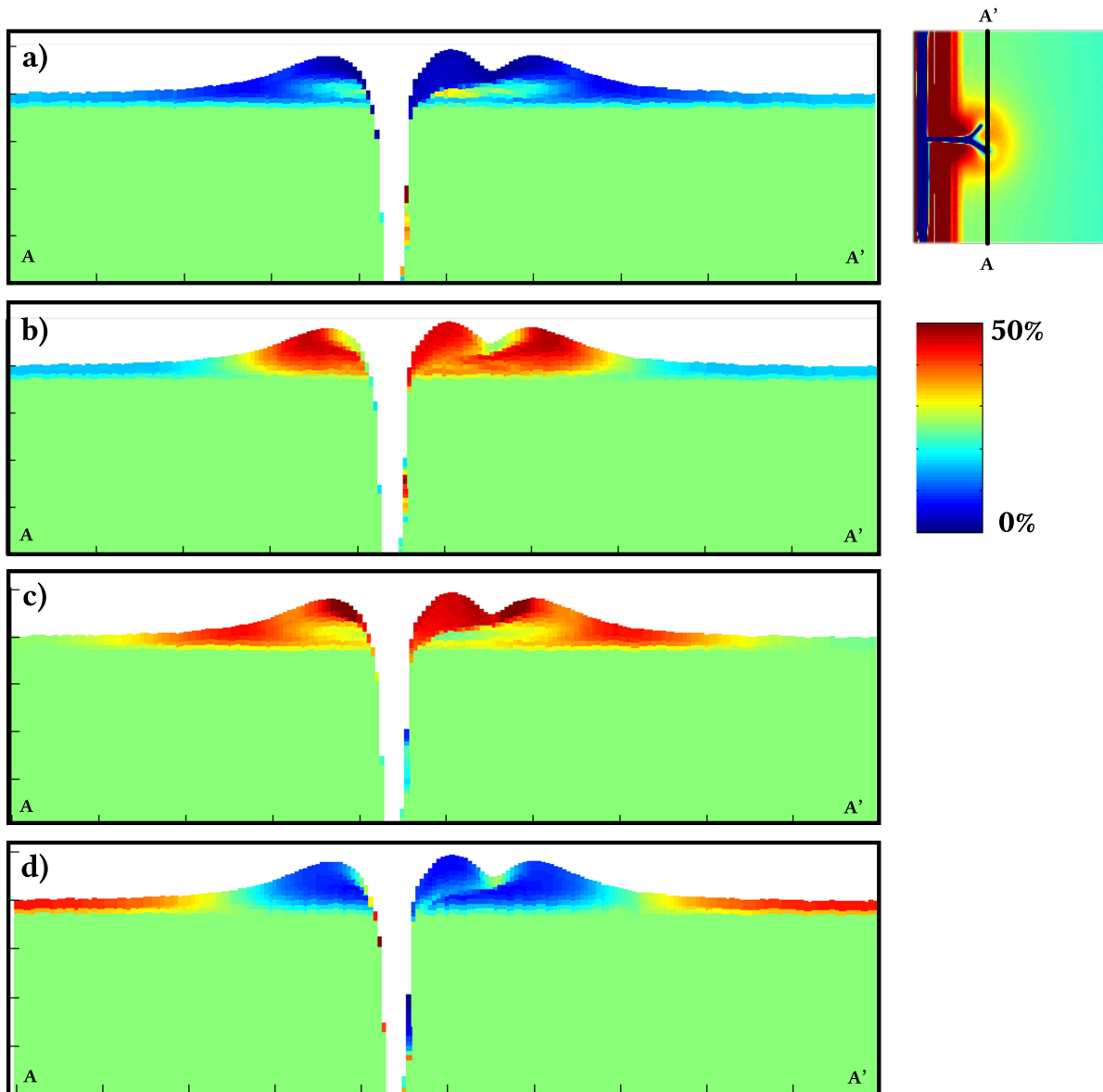


Figure 44: Volume fractions of different discrete grain-size classes. A,B,C,D have a particle diameter of 80,45,25,7  $\mu\text{m}$  respectively. The scale of the cross sections is 500m horizontally and 50cm vertically.

## F Bathymetry 2

Model output of bathymetry 2 shows behavior conform to the flooding cycle. The levee is breached during the first cycle, but doesn't show channelized flow. Water splays on the floodplain which results in erosion close to the apex and deposition more distally. The result is a incision starting from the levee breach which is surrounded by a 3-6cm thick silt-sheet. The depth and shape of the incision and the extent and thickness of deposits are i.a. dependent on sediment properties (fig. 45). The modeled processes and resulting morphology

don't resemble the observations from the modern day system (Altiplano basin). Therefore, also due to lack of time, further analysis wasn't performed.

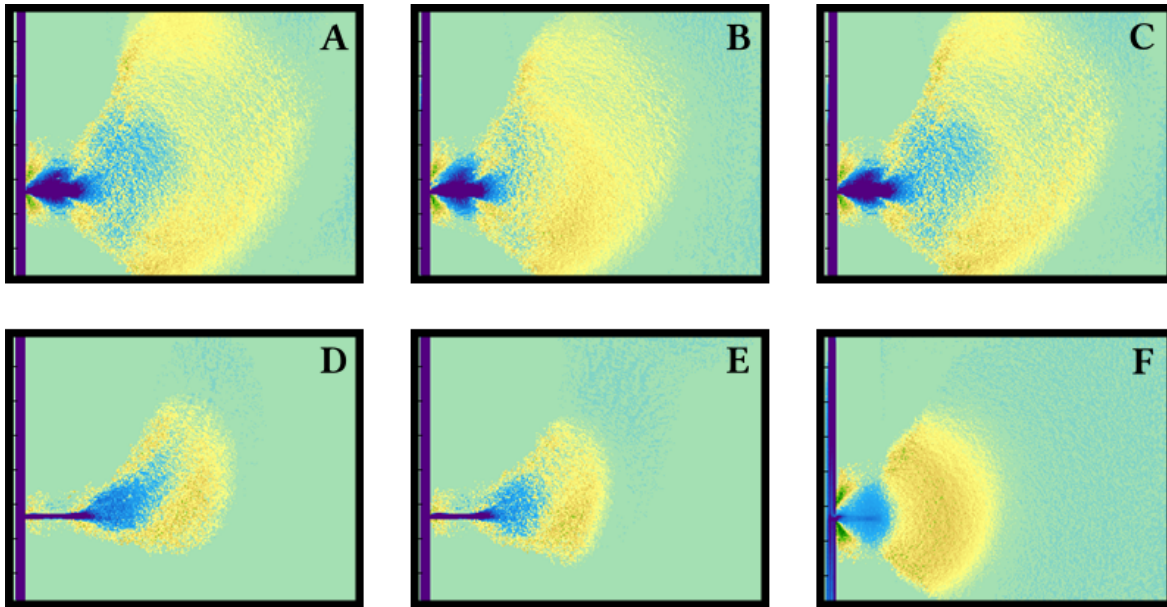


Figure 45: Results for models that started with bathymetry 2 as original morphology. The yellow/brown and blue colors represent deposition and erosion respectively. The horizontal domain comprises 1000 X 800 m. The different scenario's have different sediment properties where scenario A) is the base case, B) has higher  $\tau_{cr,e}$ , C) has higher  $V_{set}$ , D) has higher  $C_{ero}$ , E) has higher  $\tau_{cr,e}/V_{set}/C_{ero}$ , F) has higher  $\tau_{cr,e}/V_{set}$ .

## G Field Data analysis CS2 & CS24

### G.1 Splay CS2

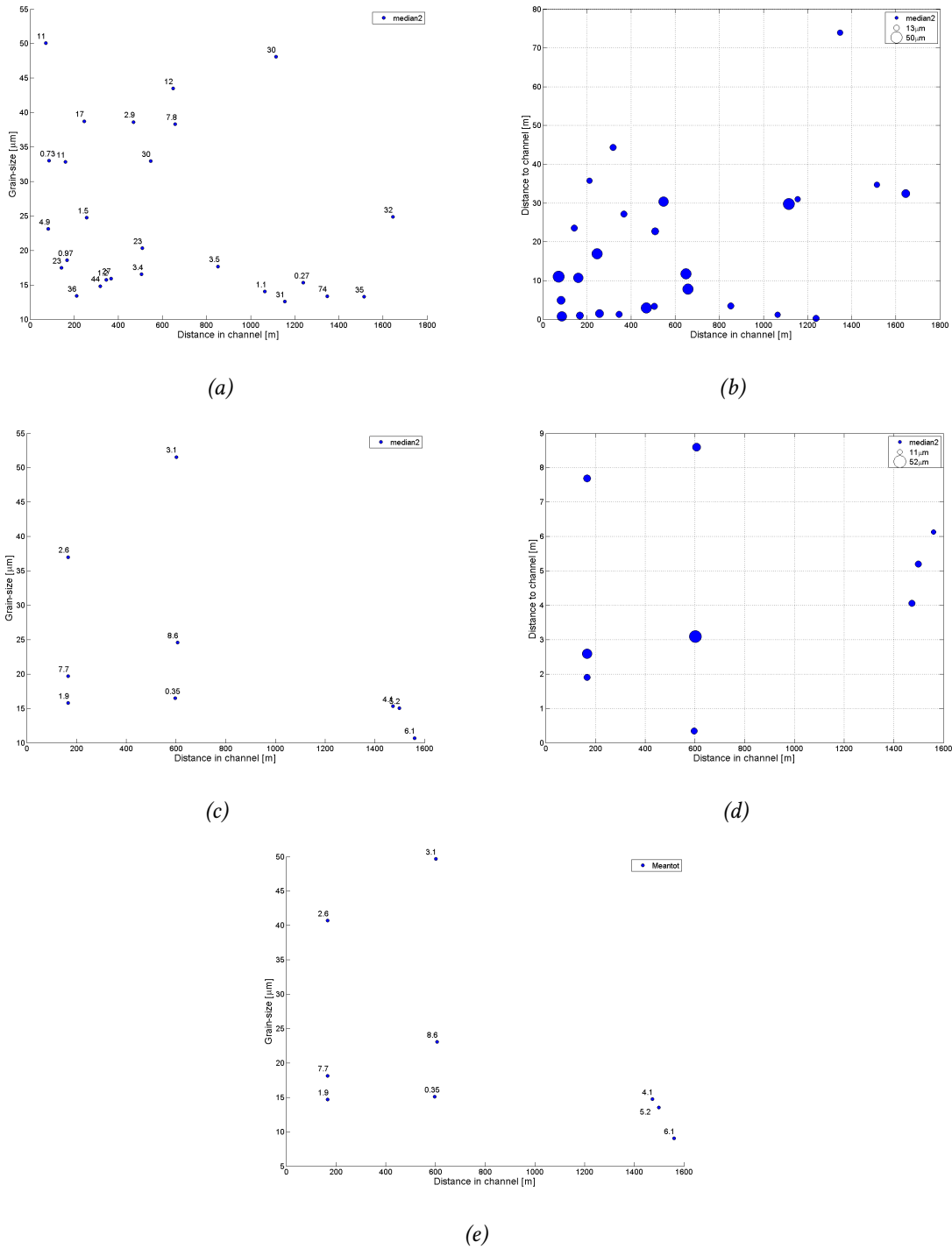


Figure 46: The result of grain-size analysis from samples originating from crevasse splay 2, sorted on depth = 10cm. A/B) The median grain size of the large fraction from the 2012 field campaign. C/D) The median grain size of the large fraction from the 2014 field campaign. E) The average grain size of the large and small fraction from the 2014 field campaign

G.2 CS24

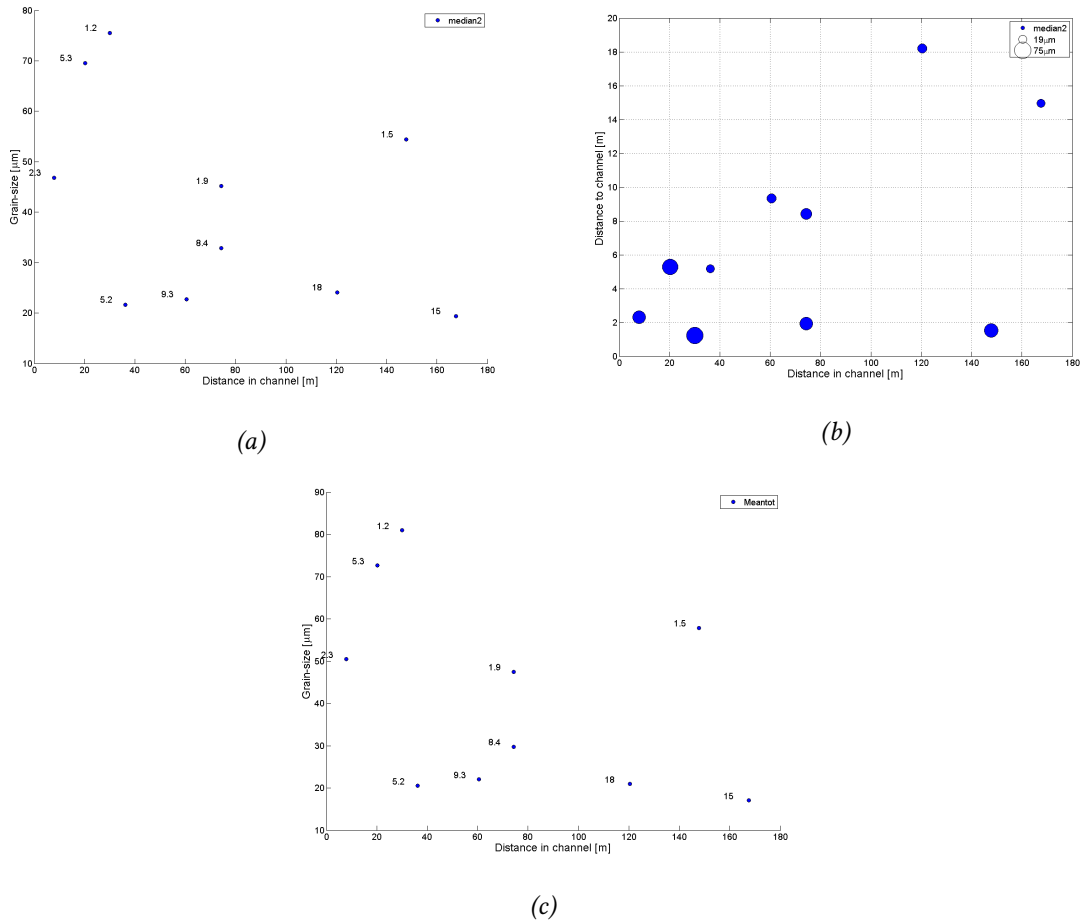


Figure 47: The result of grain-size analysis from samples originating from crevasse splay 24, sorted on depth = 10cm. They crevasse-splay was sampled in the 2014 field campaign. A/B) The median grain size of the large fraction. C) The average grain size of the large and small fraction.